

# Paramagnetic GaN:Fe and ferromagnetic (Ga,Fe)N – relation between structural, electronic, and magnetic properties

Alberta Bonanni,<sup>1</sup> Michał Kiecana,<sup>2</sup> Clemens Simbrunner,<sup>1</sup> Tian Li,<sup>1</sup> Maciej Sawicki,<sup>2</sup>  
 Matthias Wegscheider,<sup>1</sup> Martin Quast,<sup>1</sup> Hanka Przybylińska,<sup>1,2</sup> Andrea Navarro-Quezada,<sup>1</sup>  
 Rafał Jakiela,<sup>2</sup> Agnieszka Wolos,<sup>1</sup> Wolfgang Jantsch,<sup>1</sup> and Tomasz Dietl<sup>2,3,4</sup>

<sup>1</sup>*Institut für Halbleiter- und Festkörperphysik, Johannes Kepler University, Altenbergerstr. 69, A-4040 Linz, Austria*

<sup>2</sup>*Institute of Physics, Polish Academy of Sciences,  
 al. Lotników 32/46, PL 02-668 Warszawa, Poland*

<sup>3</sup>*ERATO Semiconductor Spintronics Project, Japan Science and Technology Agency,  
 al. Lotników 32/46, PL 02-668 Warszawa, Poland*

<sup>4</sup>*Institute of Theoretical Physics, Warsaw University, ul. Hoża 69, PL 00-681 Warszawa, Poland*  
 (Dated: June 8, 2018)

We report on the metalorganic chemical vapor deposition (MOCVD) of GaN:Fe and (Ga,Fe)N layers on c-sapphire substrates and their thorough characterization *via* high-resolution x-ray diffraction (HRXRD), transmission electron microscopy (TEM), spatially-resolved energy dispersive X-ray spectroscopy (EDS), secondary-ion mass spectroscopy (SIMS), photoluminescence (PL), Hall-effect, electron-paramagnetic resonance (EPR), and magnetometry employing a superconducting quantum interference device (SQUID). A combination of TEM and EDS reveals the presence of coherent nanocrystals presumably Fe<sub>x</sub>N with the composition and lattice parameter imposed by the host. From both TEM and SIMS studies, it is stated that the density of nanocrystals and, thus the Fe concentration increases towards the surface. According to Hall effect measurements, electrons from residual donors are trapped by mid-gap Fe acceptor states in the limit of low iron content  $x \lesssim 0.4\%$ , indicating that the concentration of Fe<sup>2+</sup> ions increases at the expense of Fe ions in the 3+ charge state. This effect is witnessed by photoluminescence (PL) measurements as changes in the intensity of the Fe<sup>3+</sup>-related intra-ionic transition, which can be controlled by co-doping with Si donors and Mg acceptors. In this regime, EPR of Fe<sup>3+</sup> ions and Curie-like magnetic susceptibility are observed. As a result of the spin-orbit interaction, Fe<sup>2+</sup> does not produce any EPR response. However, the presence of Fe ions in the 2+ charge state may account for a temperature-independent Van Vleck-type paramagnetic signal that we observe by SQUID magnetometry. Surprisingly, at higher Fe concentrations, the electron density is found to increase substantially with the Fe content. The co-existence of electrons in the conduction band and Fe in the 3+ charge state is linked to the gradient in the Fe concentration. In layers with iron content  $x \gtrsim 0.4\%$  the presence of ferromagnetic signatures, such as magnetization hysteresis and spontaneous magnetization, have been detected. A set of precautions has been undertaken in order to rule out possible sources of spurious ferromagnetic contributions. Under these conditions, a ferromagnetic-like response is shown to arise from the (Ga,Fe)N epilayers, it increases with the iron concentration, it persists up to room temperature, and it is anisotropic – *i.e.*, the saturation value of the magnetization is higher for in-plane magnetic field. We link the presence of ferromagnetic signatures to the formation of Fe-rich nanocrystals, as evidenced by TEM and EDS studies. This interpretation is supported by magnetization measurements after cooling in- and without an external magnetic field, pointing to superparamagnetic properties of the system. It is argued that the high temperature ferromagnetic response due to spinodal decomposition into regions with small and large concentration of the magnetic component is a generic property of diluted magnetic semiconductors and diluted magnetic oxides showing high apparent Curie temperature.

PACS numbers: 75.50.Pp, 75.30.Hx, 75.50.Tt, 81.05.Ea

## I. INTRODUCTION

In recent years, it has become more and more clear that wide band-gap semiconductors and oxides doped with transition metals (TM) constitute a new class of material systems exhibiting magnetic properties whose origin and methods of control are still not understood.<sup>1,2,3,4,5</sup> To this category belongs certainly (Ga,Fe)N, which is the subject of the present work. While extensive studies have been conducted on (Ga,Mn)N<sup>2,5,6,7</sup> as promising workbench for future applications in spintronics,<sup>8,9</sup> only little is known about the (Ga,Fe)N materials system.

The magnetic properties of nominally undoped and *p*-doped GaN implanted with Fe ions were reported, showing a ferromagnetic response evidenced by magnetization hysteresis loops persisting, depending on the provided dose,<sup>10</sup> up to room temperature (RT).<sup>11,12</sup> Furthermore, the emission channeling technique applied to Fe-implanted (Fe dose up to 10<sup>19</sup> cm<sup>-3</sup>) GaN samples confirmed the presence of a high percentage of TM ions (up to 80%) occupying substitutional Ga sites of the host crystal.<sup>13</sup> Moreover, GaN films doped with Fe, with concentrations up to 3 × 10<sup>19</sup> cm<sup>-3</sup> were grown by molecular beam epitaxy (MBE) at substrate tempera-

tures  $T_S$  ranging from 20 to 380°C directly on sapphire (0001) and ferromagnetic behavior with a Curie temperature  $T_C = 100$  K has been observed only in the samples grown at 400°C.<sup>14</sup> Films of GaN:Fe (Fe density up to  $6 \times 10^{21} \text{ cm}^{-3}$ ) fabricated by means of MBE at  $T_S = 500 - 800^\circ\text{C}$  showed a superparamagnetic behavior<sup>15,16</sup> assigned to Ga-Fe and/or Fe-N inclusions. Extended x-ray absorption fine structure (EXAFS) analysis suggests that the decrease of  $T_C$  leads to a structural transition from the wurtzite (wz) to the zinc-blende (zb) reconstruction, and this transition may be related to the origin of ferromagnetism in Fe-doped GaN films.<sup>17</sup> The metalorganic chemical vapor deposition (MOCVD) of GaN:Fe has been previously reported, with a focus on the actual Fe content in the layers and its effect onto the carrier concentration.<sup>18</sup> More recent preliminary works by others<sup>19</sup> and us<sup>20,21</sup> indicate that MOCVD grown (Ga,Fe)N shows ferromagnetic-like characteristics to above room temperature. Moreover, diluted magnetic semiconductors, and (Ga,Fe)N in particular, have become model systems to test various implementations of the density functional theory to disordered strongly correlated systems.<sup>22,23,24,25</sup>

Despite the mentioned previous reports, a thorough characterization of this novel materials system, with special attention to the mechanisms of the magnetic response, is still needed. In order to predict the feasibility of e. g. carrier-mediated spin coupling, it is crucial to know the electronic and spin structure of the TM centers, which depends on the actual charge state and is strongly influenced by the host crystal. Concerning the position of the deep acceptor-like level  $\text{Fe}^{3+}/\text{Fe}^{2+}$  in the GaN gap, it was estimated from photoluminescence (PL) excitation spectroscopy studies to be 2.5 – 2.6 eV above the GaN valence band edge  $E_v$ .<sup>26,27</sup> However, another group suggests that this level may lie much closer to the conduction band at  $(E_v + 2.863) \pm 0.005 \text{ eV}$ .<sup>28</sup>

The present work is devoted to a comprehensive study of the GaN:Fe (below the solubility limit of Fe into GaN) and (Ga,Fe)N material systems, beginning with a careful on-line control of the growth process and proceeding with a possibly thorough investigation of the structural, electrical, optical, and magnetic properties in order to shed new light into the mechanisms responsible for the paramagnetic and high-temperature ferromagnetic response of these novel systems. Particular attention is paid to avoid contamination of the superconducting quantum interference device (SQUID) signal by spurious effects and, thus, to reliably determine the magnetic properties of (Ga,Fe)N. By combining various characterization techniques, we establish experimentally the relation between structural, electronic, and magnetic properties of the studied material. We show how doping over the solubility limit affects the sample morphology and magnetic ion distribution, which in turn affect in a dramatic way both electronic and magnetic properties of the system. The interpretation of our results in terms of spinodal decomposition and non-uniform distribution of magnetic

nanocrystals along the growth direction can be applied to explain ferromagnetic-like properties persisting up to high temperatures in a broad class of diluted magnetic semiconductors and diluted magnetic oxides.

Our paper is organized as follows. In the next section we describe the experimental methods employed to characterize *in-situ* and *ex-situ* the structural, optical, transport and magnetic properties of the MOCVD structures under investigation. Section III contains a summary of sample parameters, including Fe concentrations, as determined by various experimental methods. In Sec. IV we present experimental results starting from findings obtained from transmission electron microscopy (TEM) and spatially-resolved energy dispersive X-ray spectroscopy (EDS). These measurements reveal a highly non-uniform distribution of the magnetic ions at Fe concentrations surpassing the solubility limit. We then discuss how the presence of magnetic nanocrystals and the non-uniformity in their distribution modify the electrical, optical, magnetic resonance, and magnetic characteristics of the system. Conclusions and outlook stemming from our work are summarized in Sec. V. Finally, in Appendix, we discuss in detail the procedure employed to determine reliably the magnetic response of (Ga,Fe)N by SQUID magnetometry.

## II. EXPERIMENTAL

### A. Growth procedure

The studied epilayers have been fabricated in an AIXTRON 200RF horizontal-tube MOCVD reactor. All structures have been deposited on c-plane sapphire substrates according to a well established growth procedure<sup>29</sup> involving TMGa,  $\text{NH}_3$ ,  $\text{Cp}_2\text{Mg}$ ,  $\text{SiH}_4$ , and  $\text{Cp}_2\text{Fe}$  as precursors for respectively Ga, N, Mg, Si, and Fe, with  $\text{H}_2$  as a carrier gas. Upon the nitridation of the substrate in the reactor, the deposition of a low-temperature (540 °C) GaN nucleation layer (LT-NL), its annealing under  $\text{NH}_3$  and the growth of a 1  $\mu\text{m}$  thick device-quality GaN layer at 1050°C, as a first step, several series of 500 nm thick GaN:Fe at different substrate temperatures (ranging from 750 to 1050°C) and different  $\text{Cp}_2\text{Fe}$  flow rates [between 50 and 400 standard cubic centimeters per minute (sccm)] have been fabricated. The nominal Fe content in subsequently grown samples has been alternatively switched from low to high and *vice-versa*, in order to minimize long term memory effects due to the presence of residual Fe in the reactor.<sup>30</sup> The samples have been continuously rotated during growth to promote the deposition homogeneity.

## 2. In-situ X-ray diffraction

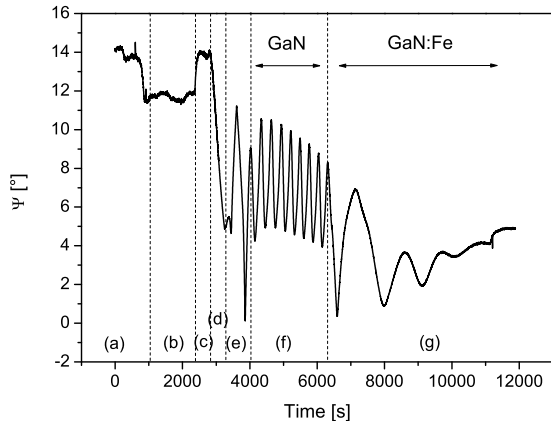


FIG. 1: *In-situ* ellipsometry: ellipsometric angle  $\Psi$  at 2 eV as a function of time for a standard deposition sequence. Particular regions relative to the growth process and marked (a) to (g) are discussed in the main text.

### B. In-situ monitoring

#### 1. Spectroscopic ellipsometry and laser interferometry

The employed MOCVD reactor is equipped with an *in-situ* Isa Jobin Yvon ellipsometer which allows both spectroscopic (optical response – in terms of the ellipsometric angles  $\Psi$  and  $\Delta$  – as a function of the photon energy) and kinetic (optical response as a function of time) on-line measurements over the energy range between 1.5 and 5.5 eV for process optimization.<sup>31</sup> Figure 1 shows the ellipsometric angle  $\Psi$  at 2 eV as a function of time for the standard growth process employed to fabricate the samples under investigation: (a) heating of the sapphire substrate from RT to 1200°C; (b) desorption under  $H_2$  flow to stabilize the surface; (c) cooling and nitridation of the substrate; (d) deposition of the LT-NL; (e) annealing of the NL; (f) growth of the GaN buffer layer; (g) growth of the Fe doped GaN layer. Spectroscopic ellipsometry measurements carried out in real time allow the on-line control over the growth-rate and the composition of the growing layer and provide additional qualitative information on the surface roughness. Moreover, simultaneously to ellipsometry, standard on-line dynamic optical reflectivity<sup>32</sup> at 2 eV has been routinely performed, yielding analogous information on the growing layer as ellipsometry, but being more sensitive to wobbling (unavoidable during the MOCVD process) and temperature effects.<sup>33</sup>

Furthermore, the growth process has been routinely monitored *in-situ* by x-ray diffraction. In addition to the optical windows necessary for the on-line ellipsometry characterization, the MOCVD reactor has been implemented with two Be windows transparent to the radiation energy provided by a PANalytical Cu x-ray tube. A Johansson monochromator focuses the beam on the growing crystal in a geometry suitable for the observation of the (11 $\bar{2}$ 4) reflection of wz-GaN. The diffracted beam is collected by a multichannel detector PANalytical X'Celerator with an angular resolution of 0.013° per pixel in this geometry. This diffraction set-up allows us to perform kinetic measurements yielding information on the layer composition, thickness and crystalline quality even on rotating samples, thanks to a recently developed wobbling compensation algorithm.<sup>34,35</sup> Moreover, real time reciprocal space mapping can be carried out in a wide temperature range (20 – 1050°C), though limited to a static sample configuration, in order to eliminate wobbling effects.<sup>36</sup>

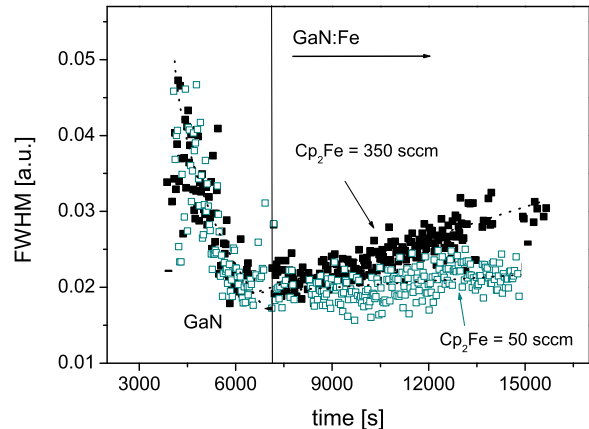


FIG. 2: *In-situ* XRD kinetic measurement: FWHM of the (11 $\bar{2}$ 4) GaN reflection vs. deposition time for two samples grown with different  $Cp_2Fe$  flow rates. The evolution of the FWHM during the growth of the GaN buffer is reproducibly independent of the sample, whereas the broadening during the deposition of the Fe-containing layer is a function of the magnetic ions content.

Kinetic *in-situ* XRD measurements were routinely carried out during growth. A full-width-at-the-half maximum (FWHM) analysis of the GaN peak in the *in-situ* spectra as a function of the growth time, yields information on the crystal quality of the layers. In Fig. 2 a clear decrease of the FWHM during the deposition of the GaN buffer due to the growing thickness of high crystalline quality GaN is detectable and was proven to be quantitatively reproducible on a full series of samples.<sup>34</sup> The vertical line demarcates the time corresponding to

the opening of the  $\text{Cp}_2\text{Fe}$  source and indicates the onset of broadening of the GaN peak due to the incorporation of Fe ions. A clear dependence of the FWHM on the layer thickness and on the iron precursor flow rate is evident and comparable to the values obtained from *ex-situ* post-growth XRD analysis reported in Table I.

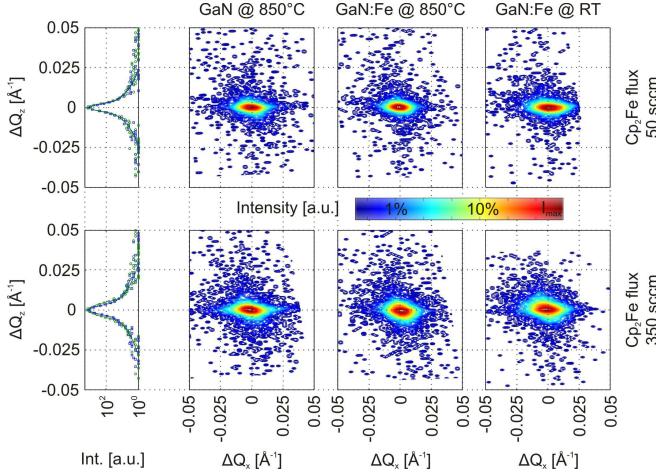


FIG. 3: *In-situ* XRD space maps in the  $(11\bar{2}4)$  reflection of GaN and broadening in the inverse of the lattice parameter along the growth direction (left panels) for two values of  $\text{Cp}_2\text{Fe}$  flow rates, 50 and 350 sccm (upper and lower panel, respectively).

A more detailed information on the structural properties of the layers, can be obtained by acquiring *in-situ* reciprocal space maps. The diffraction geometry for the observation of the  $(11\bar{2}4)$  reflection has been chosen in such a way that the sensitivity to the lattice parameter  $Q_z$  perpendicular to the  $(0001)$  surface could be optimized. After the deposition of the GaN buffer the substrate rotation was interrupted at the proper azimuth for the acquisition of reciprocal space maps. Figure 3 presents the space map for the GaN buffer layer (GaN @ 850°C) qualitatively reproducible for all investigated samples. The procedure was repeated just after the deposition of the Fe-doped layer (GaN:Fe @ 850°C) and after cooling the sample to room temperature (GaN:Fe @ RT) upon completion of the growth process. The reciprocal maps in Fig. 3 evidence the variation of the lattice parameter along the growth direction,  $\Delta Q_z$ , obtained from the following relation,<sup>34</sup>

$$\Delta Q_z = \frac{2\pi}{\lambda} \cdot \cos(\epsilon_{\text{GaN}}) \cdot \Delta\epsilon; \quad (1)$$

where  $\lambda$  is the wavelength of the incident radiation,  $\epsilon_{\text{GaN}}$  gives the diffraction angle for relaxed GaN and  $\Delta\epsilon$  is the measured relative peak position. As confirmed by *in-situ* kinetic measurements and post growth analysis, the broadening is a function of the iron flow rate.

## C. Ex-situ characterization methods

### 1. High-resolution X-ray diffraction

High-resolution X-ray diffraction (HRXRD) rocking curves of the GaN (0002) reflex, give for all the samples, including the (Ga,Fe)N structures, a FWHM of 200 – 320 arcsec, comparable with state-of-the-art device-quality gallium nitride material.<sup>37</sup> The broadening of the GaN(0002) reflex is found to depend both on the iron doping level and on the growth temperature. The minimum FWHM is obtained for the lowest  $\text{Cp}_2\text{Fe}$  flow rate, 50 sccm, and the highest growth temperature, 950°C. Despite the importance of HRXRD for the routine structural characterization of the layers, the inadequacy of standard X-ray diffraction methods for nanoscale investigations (detection of the presence of non-uniform magnetic ion distribution) is already widely accepted.<sup>5</sup> We also note that, according to atomic force microscopy (AFM), the surface roughness increases with the Fe concentration, an effect that may affect some quantitative considerations. The change in sample morphology indicates the onset of a three-dimensional (3D) granular-like growth mode characterized by grain height differences exceeding the layer nominal thickness at the highest Fe concentration.

### 2. Secondary-ion mass spectroscopy

The total Fe concentration in the layers has been determined via secondary-ion mass spectroscopy (SIMS) and calibrated with an undoped GaN sample implanted with  $10^{16} \text{ cm}^{-2}$   $^{56}\text{Fe}$  at 270 keV as reference. The total Fe concentration in the layers is found to increase with the nominal  $\text{Cp}_2\text{Fe}$  flow rate. We also detect an increase in the oxygen concentration which reaches  $10^{20} \text{ cm}^{-3}$  at the highest  $\text{Cp}_2\text{Fe}$  flow rates, an effect that may result from a larger surface area due to the above-mentioned onset of granular growth. We underline that the granular morphology may render the quantitative determination of Fe and O contents and profiles not reliable in the case of the highest Fe concentration.

### 3. Electron-paramagnetic resonance

Electron paramagnetic resonance (EPR) data have been acquired with a BRUKER ELEXSYS E-580 spectrometer, operating at a frequency of 9.48 GHz (X-band). The spectrometer is equipped with a continuous-flow Oxford cryostat, enabling measurements in the temperature range 2 – 300 K.

#### 4. Photoluminescence

The photoluminescence (PL) measurements in ultra-violet (UV) regime have been carried out in a set-up consisting of a Helium Cadmium (HeCd) laser with a wavelength of 325 nm (3.82 eV) and an excitation power of 40 mW, a Jobyn Yvon monochromator with a focal length of 550 mm and a Jobyn Yvon 1024  $\times$  512 pixel liquid nitrogen-cooled Charge Coupled Device (CCD) camera for detection. For the measurements in the infrared (IR) region the 351.1 nm (3.53 eV) line of a Spectra Physics argon-laser, a Spex Spectrometer with 850 mm focal length and a liquid nitrogen cooled Ge-detector were employed. In both set-ups, the samples were placed in a He-cooled flow cryostat, which allows to cool the samples to 5 K. For adjusting the temperature a silicon diode and a Lakeshore 331 temperature controller were employed.

#### 5. Magnetic characterization

The magnetic properties have been investigated in a home made 1 T SQUID magnetometer working in the temperature range 5 - 330 K. The samples for magnetic investigations are typically cut into  $9 \times 3$  or  $5 \times 5$  mm<sup>2</sup> pieces, for in-plane and both in- and out-of-plane comparative measurements, respectively. We study both the temperature dependence of the magnetization at a constant field and the sample response to the variation of the external field at a constant temperature. In this case, we find it sufficient to sweep the field in one direction only – a half hysteresis loop – and to obtain the second half by means of numerical reflection of the data. Selected measurements of the full hysteresis loop have been carried out in order to ensure the reliability of this experimental procedure. Also, all the magnetization data presented in the paper are already corrected for the diamagnetic signal from the substrate, reflecting, in this way, the properties of the investigated layers only. A detailed discussion of the subtraction procedure and related experimental difficulties specific to magnetic measurements on thin films of diluted magnetic semiconductors and the precautions undertaken in the present work are outlined in the Appendix.

#### 6. Transmission electron microscopy

Transmission electron microscopy studies have been carried out on cross-sectional samples prepared by standard mechanical polishing followed by Ar<sup>+</sup> ion milling at 4 kV for about 1 h. Conventional diffraction contrast images in bright-field imaging mode and high-resolution phase contrast pictures were obtained from a JEOL 2011 Fast TEM microscope operating at 200 kV and capable of an ultimate point-to-point resolution of 0.19 nm and allowing to image lattice fringes with a 0.14 nm resolution.

The energy dispersive x-ray analysis has been performed *via* an Oxford Inca EDS equipped with a silicon detector.

### III. SAMPLE PARAMETERS

In Table I we summarize the data related to the GaN:Fe, (Ga,Fe)N and reference GaN samples considered in this work. As already mentioned, all samples have been grown on c-sapphire substrates. The Fe-doped structures consist of a nominally 500 nm thick GaN:Fe or (Ga,Fe)N layer deposited onto a 1  $\mu$ m thick GaN buffer, whereas the reference samples are mere 1  $\mu$ m thick GaN buffers (nominally undoped) on sapphire. In the table, the following values are listed: the Cp<sub>2</sub>Fe flow rate employed to grow the TM-doped layers, the FWHM of the (0002) reflex from GaN determined by *ex-situ* HRXRD, the Fe<sup>3+</sup> concentration according to SQUID data and evaluated from the Curie constant (in the case of low Fe concentration, where the low-temperature paramagnetic contribution is not covered by the ferromagnetic signal) and from the saturation value of the ferromagnetic magnetization, respectively. The sample numbers in the figures throughout the paper refer to Table I.

### IV. EXPERIMENTAL RESULTS AND DISCUSSION

#### A. Transmission electron microscopy

According to our TEM studies, in the limit of low Fe-doping, *i.e.*, for Cp<sub>2</sub>Fe flow rates in the range 50 – 150 sccm the structure of the GaN matrix is not detectably affected. As indicated in Fig. 4, the lattice spacing between the (0002) planes is  $0.250 \pm 0.010$  nm, perfectly matching that of undoped GaN. In addition, the EDS spectra do not point to Fe aggregation (Fig. 5), indicating that the Fe ions are randomly distributed over the lattice, presumably in substitutional sites of Ga. Above 175 sccm, however, TEM studies reveal the presence of nanocrystals embedded in the host GaN.

According to the TEM micrographs presented in Figs. 6(a) and (b), the precipitates are located both close to the surface and inside the epilayer in dislocation-free regions, suggesting that precipitation is not related to the presence of dislocations. On the other hand, Figs. 6(c) and (d) prove that some nanocrystals are embedded into the upper surface layers, while some others are decorating the screw- or mixed- type threading dislocations in a volume proximal to the surface. Furthermore, EDS spectra demonstrate that the concentration of Fe ions is largely enhanced within the nanocrystals. As shown in Fig. 7, the Fe-*K* <sub>$\alpha$ 1</sub> peak at 6.404 KeV can be seen clearly in the spectrum taken in the region of a precipitate, while in the adjacent areas, the presence of Fe is not detected. It should be mentioned that the precipitates can be found only in the upper region of the layer within

TABLE I: Data related to the investigated GaN, GaFe:N and (Ga,Fe)N samples. The following values are listed: the  $\text{Cp}_2\text{Fe}$  flow rate employed to grow the Fe-doped layers, the FWHM of the (0002) reflex from GaN determined by *ex-situ* HRXRD, the Fe concentration according to the Curie constant from SQUID data (in the case of low Fe concentration, where the Curie component is not covered by the ferromagnetic signal;  $S = 5/2$  and  $g = 2$  is assumed) and from the saturation value of ferromagnetic magnetization  $M_S$ , assuming  $S = g = 1$ .

sample number	$\text{Cp}_2\text{Fe}$ flow rate [sccm]	FWHM [arcsec]	$\text{Fe}^{3+}$ conc. Curie comp. [ $\text{cm}^{-3}$ ]	$M_S/\mu_B$ [ $\text{emu}/(\text{cm}^3\mu_B)$ ]	sample number	$\text{Cp}_2\text{Fe}$ flow rate [sccm]	FWHM [arcsec]	$\text{Fe}^{3+}$ conc. Curie comp. [ $\text{cm}^{-3}$ ]	$M_S/\mu_B$ [ $\text{emu}/(\text{cm}^3\mu_B)$ ]
#310	0	265	—	—	#467	175	279	—	$3.02 \times 10^{19}$
#486	0	220	—	—	#320	200	323	$4.5 \times 10^{19}$	$1.05 \times 10^{19}$
#329	0 (GaN:Mg)	287	—	—	#470	200	258	—	$2.26 \times 10^{19}$
#317	50	289	$1.8 \times 10^{19}$	—	#472	225	282	—	$2.37 \times 10^{19}$
#367	50	272	$1.2 \times 10^{19}$	$8.41 \times 10^{18}$	#469	250	269	—	$6.15 \times 10^{19}$
#371	50	220	$1.4 \times 10^{19}$	0	#473	275	307	—	$5.82 \times 10^{19}$
#409	50	249	—	$1.2 \times 10^{19}$	#471	300	316	—	$7.66 \times 10^{19}$
#318	100	288	$1.9 \times 10^{19}$	—	#468	325	320	—	$8.84 \times 10^{19}$
#319	150	308	$2.3 \times 10^{19}$	$6.47 \times 10^{18}$	#466	350	302	—	$8.95 \times 10^{19}$
#465	150	294	—	—	#408	400	305	—	$2.25 \times 10^{20}$

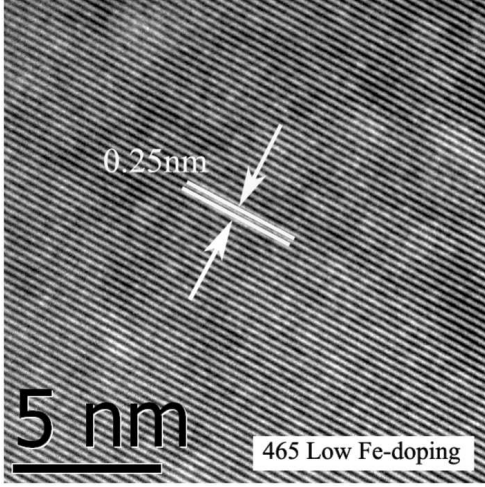


FIG. 4: HRTEM lattice fringe image of the (0002) planes demonstrating that low Fe-doping (sample #465) does not cause detectable strain, the lattice parameter ( $d_{0002} = 0.25 \pm 0.01$  nm) being the same as that of undoped GaN.

300 nm from the surface, and thus well above the interface between the nominally undoped GaN buffer and the Fe-doped layer. The segregation of TM-rich nanocrystals towards the surface of the samples, seems to represent a general phenomenon in highly TM-doped MOCVD III-V compounds: a similar effect has been observed for MnAs nanocrystals in MOCVD grown (Ga,Mn)As.<sup>38</sup>

We estimate that the nanocrystals occupy less than

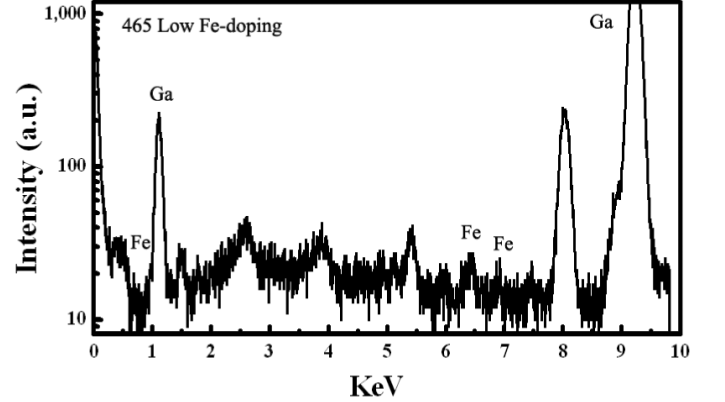


FIG. 5: EDS spectrum showing the presence of Fe in the measured regions of the GaN layers doped with a low concentration of Fe ions (sample #465).

1% of the film volume and their diameter varies from 5 to 50 nm. Some precipitates are elongated in the growth direction, as shown in Fig. 8(a), such a behavior being expected within the spinodal decomposition scenario<sup>39</sup>. This non-spherical shape may lead to an additional magnetic anisotropy that can elevate the blocking temperature. In Fig. 8(b) the selected area diffraction pattern (SADP) along the  $(10\bar{1}0)$  zone axis taken around the precipitate in Fig. 8(a) is shown. It reveals the presence of an additional hexagonal phase with almost the same orientation as the GaN matrix. In the corresponding schematic indexed pattern (Fig. 8(c)) closed circles cor-

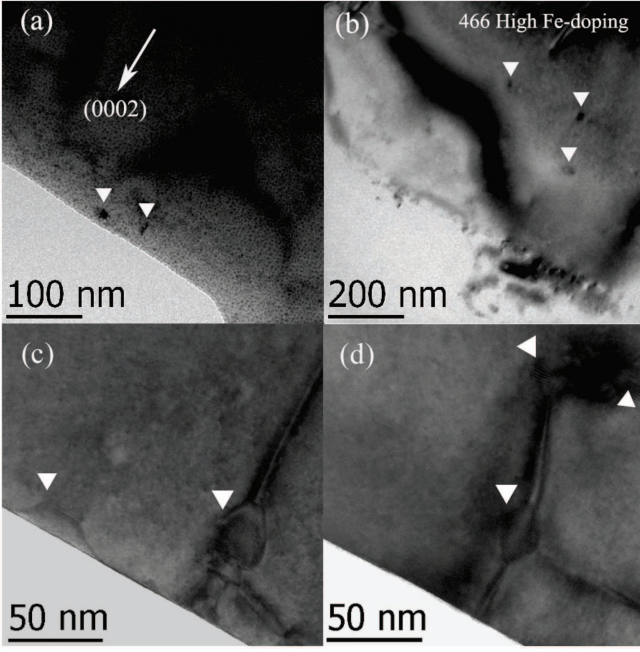


FIG. 6: Bright-field transmission electron micrographs of (Ga, Fe)N demonstrating the presence of precipitates as indicated by the white triangles (a) close to the surface and (b) in the mid of the epilayer. Some precipitates (c) are embedded into the surface and others, (c) and (d) sink to the dislocations.

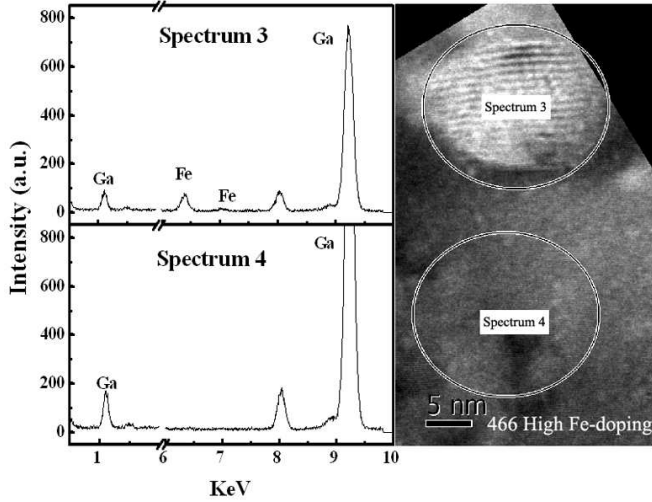


FIG. 7: EDS spectra for the sample #466 (left panel) taken around the precipitate (right panel) showing that the concentration of Fe is significantly enhanced in the region of the precipitate (recorded as spectrum 3) as compared with the surrounding matrix (recorded as spectrum 4).

respond to GaN, open circles to the additional phase and crosses to the double diffraction between them. The lattice parameters of this new phase are  $a = 0.268 \pm 0.010$  nm,  $c = 0.436 \pm 0.010$  nm. By comparing the lattice constants to those of Fe and iron nitride nanostructures and thin films listed in Table II, we tend to believe that

$\epsilon$ -Fe<sub>3</sub>N is formed in the considered precipitates. However, it is also expected that the GaN host can stabilize Fe<sub>x</sub>N or (Ga,Fe)<sub>x</sub>N nanocrystals in a form not existing in the case of nanostructured Fe-N material systems. Actually, such a situation has recently been revealed in the case of MBE grown (Ge,Mn), where spinodal decomposition into Ge and novel Mn-rich (Ge,Mn) nanocrystals has been found.<sup>40</sup>

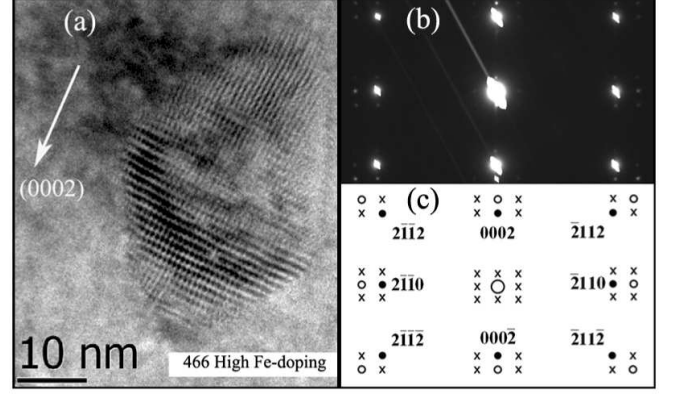


FIG. 8: (a) Elongated precipitate observed in an HRTEM image of Moiré fringes contrast. (b) SADP pattern acquired in the region around the precipitate along the  $(10\bar{1}0)$  zone axis; (c) the corresponding schematic graph for indexing of the diffraction spots.

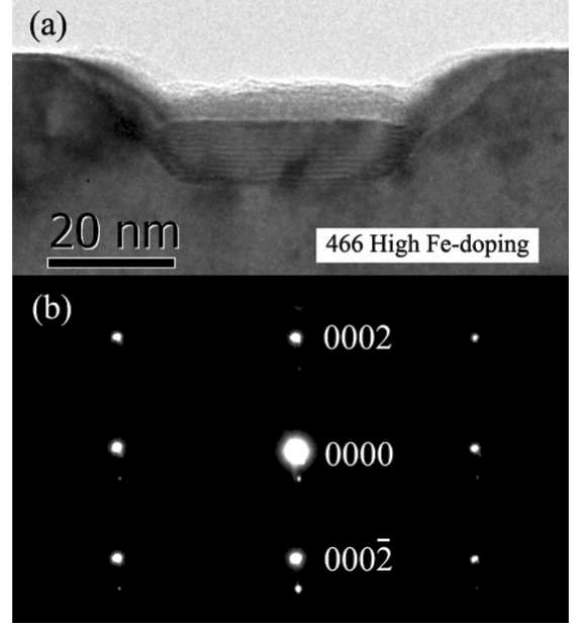


FIG. 9: (a) HRTEM image of a precipitate residing on the surface of a highly Fe-doped sample (#466); (b) the corresponding SADP pattern along the  $(10\bar{1}0)$  zone axis.

Our HRTEM studies allow to detect also precipitates residing at the surface of the highly Fe-doped samples, as shown in Fig. 9(a). The SADP pattern in Fig. 9(b) sug-

TABLE II: Structural and magnetic parameters of some iron and iron-nitride phases in nanostructures and thin films. To be compared with our experimental values.

		lattice parameter		
	structure	$a(\text{nm})$	$c(\text{nm})$	$\mu_B$
FeN	ZB	0.430 <sup>a</sup>	–	AF or 0 <sup>a</sup>
	RS	0.40 <sup>b</sup>	–	–
$\gamma'$ -Fe <sub>4</sub> N	RS	0.382 <sup>b</sup>	–	2.21 <sup>a</sup>
$\gamma''$ -FeN <sub>0.91</sub>	ZB	0.433 <sup>a</sup>	–	1.7 or 0 <sup>a</sup>
$\varepsilon$ -Fe <sub>3</sub> N	WZ	0.270 <sup>c</sup>	0.433 <sup>c</sup>	1.9 <sup>d</sup>
$\gamma'''$ -FeN <sub>0.5–0.7</sub>	RS	0.450 <sup>a</sup>	–	ferro <sup>a</sup>
$\varsigma$ -Fe <sub>2</sub> N	HCP	0.443 <sup>a</sup>	0.484 <sup>a</sup>	para/1.5 <sup>h</sup>
$\gamma$ -Fe	ZB	0.361-0.370 <sup>e</sup>	–	0.3-2.0 <sup>e</sup>
$\alpha$ -Fe	BCC	0.286 <sup>f</sup>	–	2.2 <sup>g</sup>

<sup>a</sup>Reference 41 and references therein

<sup>b</sup>Reference 42

<sup>c</sup>Reference 43

<sup>d</sup>Reference 44

<sup>e</sup>Reference 45

<sup>f</sup>Reference 46

<sup>g</sup>Reference 47

<sup>h</sup>Reference 48

gests that the Moiré fringes in this precipitate (Fig. 9(a)) are formed by the interference of the GaN (0002) planes of the matrix crystal with a set of lattice planes parallel to (0002) with a  $d$ -spacing of  $0.204 \pm 0.010$  nm, which is almost the same as that of the (111) planes of  $\gamma$ -Fe or of the (110) planes of  $\alpha$ -Fe, as reported in Table II. Therefore, these precipitates segregating to the surface could consist of pure iron, this assumption being consistent with the evaporation of nitrogen from the surface during the MOCVD process and with the consequent hindering of the Fe-nitride compounds formation.

One may expect that the highly non-uniform Fe distribution over the layer volume shown by TEM investigations will have a dramatic influence on the electronic and magnetic properties of (Ga,Fe)N. Experimental results presented in the next sub-sections confirm this conjecture.

## B. Electrical properties

It has been found previously that Fe doping reduces the electron concentration in GaN and leads to a semi-insulating material.<sup>49,50,51</sup> In order to find out how the electronic properties evolve when the Fe concentration surpasses the solubility limit, we have undertaken electrical and optical measurements. Together with EPR spectroscopy, such studies allow us to assess the charge and spin state of Fe ions controlling the magnetic properties of the material system under investigation. Hall effect and resistance measurements have been carried out in the Van der Pauw geometry on  $5 \times 5$  mm<sup>2</sup> square cuts of GaN, GaN:Fe, and (Ga,Fe)N wafers, whose characteristics are summarized in Table I. Soldered indium contacts are employed and the ohmic characteristics of all contacts are carefully tested. The Hall resistance has been measured in the magnetic field  $B = \pm 500$  mT using currents in the range 10 to 200  $\mu$ A. The employed current values are high enough to achieve high Hall voltages for better accuracy, but still sufficiently low to avoid Joule heating of the sample.

In the studied samples, both the (Ga,Fe)N film and the GaN buffer layer are conducting, so that a procedure suitable for the evaluation of electrical characteristics in the presence of a parallel conducting channel has to be employed. Accordingly, in order to obtain the conductance tensor components  $G_{ij}^{(f)}$  of the (Ga,Fe)N films, the buffer contribution  $G_{ij}^{(b)}$  has to be subtracted from the total conductance  $G_{ij}$ . We evaluate  $G_{ij}^{(b)}$  and  $G_{ij}^{(f)}$  from the measured values of the square resistance  $R$  and Hall resistance  $R_{\text{Hall}}$  for the reference GaN sample and for the samples containing the (Ga,Fe)N films according to:

$$G_{xx}^{(b)} = t_b R^{(r)} / [t_r (R^{(r)^2} + R_{\text{Hall}}^{(r)^2})]; \quad (2)$$

$$G_{yx}^{(b)} = t_b R_{\text{Hall}}^{(r)} / [t_r (R^{(r)^2} + R_{\text{Hall}}^{(r)^2})]; \quad (3)$$

$$G_{xx} = R / [(R^2 + R_{\text{Hall}}^2)]; \quad (4)$$

$$G_{yx} = R_{\text{Hall}} / [(R^2 + R_{\text{Hall}}^2)]; \quad (5)$$

where  $t$ ,  $t_b$ , and  $t_r$  are the thickness of the (Ga,Fe)N film, of the buffer layer, and of the reference sample, respectively. Therefore, the (Ga,Fe)N conductance is  $G_{ij}^{(f)} = G_{ij} - G_{ij}^{(b)}$  and from that we obtain the resistivity  $\rho$  and the Hall electron concentration  $n$  of the (Ga,Fe)N films in the standard way:

$$\rho = t / G_{xx}^{(f)} (B = 0); \quad (6)$$

$$n = B (G_{xx}^{(f)^2} + G_{xy}^{(f)^2}) / (e t G_{xy}^{(f)}). \quad (7)$$

We must point out that within this model we assume the carrier concentration of the GaN buffer layer to be

the same in all the measured samples and that there is no diffusion of Fe into the buffer. Fluctuations in the buffer properties will affect the data in a significant way when the conductance of the (Ga,Fe)N layer becomes small. All the studied samples are found to be n-type with  $R_H < 0$ , where  $R_H = R_{Hall} \cdot t/B$  is the Hall constant. As shown in Fig. 10, in the region of low  $Cp_2Fe$  flow rate we find the magnitude and temperature dependencies of the Hall concentration typical for MOCVD GaN epitaxial films, in which electrons freeze-out at residual donors at low temperatures. The obtained activation energy of the carriers in GaN, namely  $E_a = 31$  meV, supports this conclusion. According to our findings summarized in Figs. 10 and 11, the samples grown at the low  $Cp_2Fe$  flow rate of 150 sccm show reduced Hall concentration as compared to GaN, which may result from trapping of the electrons by Fe ions,  $Fe^{3+} \rightarrow Fe^{2+}$ , an effect consistent with the position of the  $Fe^{3+}/Fe^{2+}$  acceptor level in the band gap of GaN, as we will discuss in more detail in the next subsection.

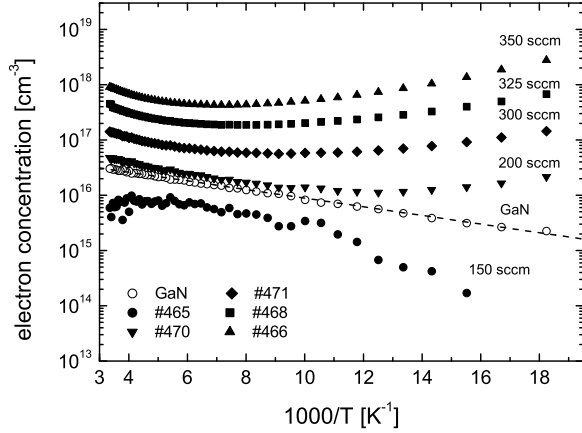


FIG. 10: Electron concentration  $n$  from Hall effect measurements as a function of the inverse temperature for a GaN layer and a series of GaN:Fe – (Ga,Fe)N samples with differing Fe content controlled by the  $Cp_2Fe$  flow rate.

Interestingly, when the  $Cp_2Fe$  flow rate exceeds 150 sccm, which according to SIMS data corresponds to a Fe content above  $10^{20} \text{ cm}^{-3}$ , we observe a strong increase of the Hall concentration, and a change in the character of its temperature dependence, a behavior clearly seen in Figs. 10 and 11. For the highest flow rate of 350 sccm, the Hall concentration reaches  $10^{18} \text{ cm}^{-3}$ , a value more than two orders of magnitude higher than that for the sample grown with the  $Cp_2Fe$  flow rate of 150 sccm. This effect might suggest the appearance of an additional conductance channel associated with the hopping of electrons between Fe ions at large magnetic ions densities. Actually, hopping conductance involving Fe impurities was discussed for InP,<sup>52</sup> where, however, the measured resistance was found to be much larger than in our case.

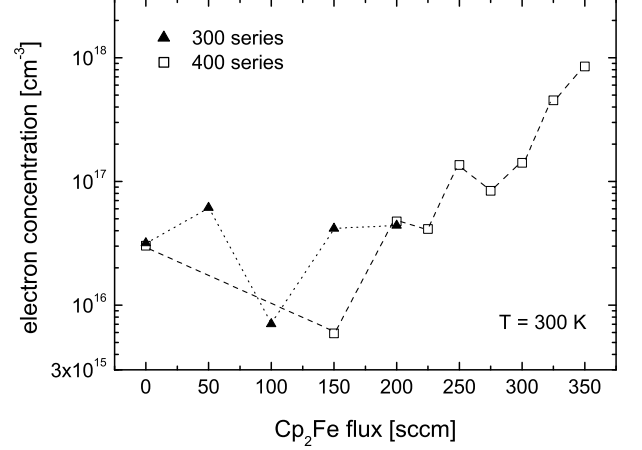


FIG. 11: Electron concentration  $n$  from Hall effect measurements as a function of the  $Cp_2Fe$  flow rate for two GaN reference layers and for two series of (GaN:Fe – Ga,Fe)N samples (triangles and squares, respectively) at room temperature. Reduced electron concentrations in the low flow rate region points to a semi-insulating character of Fe-doped layers in this regime.

Indeed, the relatively large values for the Hall mobility  $\mu = 1/(en\rho)$  shown in Fig. 12 make the hopping scenario improbable. We also note that, as discussed in subsection IV A, Fe-rich nanocrystals are formed at higher flow rates, so that we deal with carrier transport in a highly inhomogeneous medium. Under such conditions, the relation between the Hall and carrier densities becomes intricate. It is more probable that (at least a part) of the rise in the Hall concentration is caused by an increase in the oxygen donor density for large  $Cp_2Fe$  flow rates. SIMS analysis shows that the oxygen concentration increases by over two orders of magnitude upon changing the flow rate from 50 to 350 sccm and at the highest flow rate it becomes comparable to the iron concentration. Finally, it is also possible that some part of the Fe ions occupies interstitial positions in which  $Fe^{2+}$  acts as a double donor. Optical and ESR data presented in the next subsections show that the charge state of Fe ions transforms from +3 to +2 with increasing Fe concentration. This effect supports the scenario which assigns the enhancement in the carrier concentration to the increase of the donor concentration with the Fe content, though the origin of the relevant impurity or defect remains uncertain. We will return to this open question when discussing the results of the EPR measurements.

### C. Optical properties

Photoluminescence measurements in the infrared, visible, and ultra-violet regime have been carried out on the whole series of samples with increasing Fe concentration.

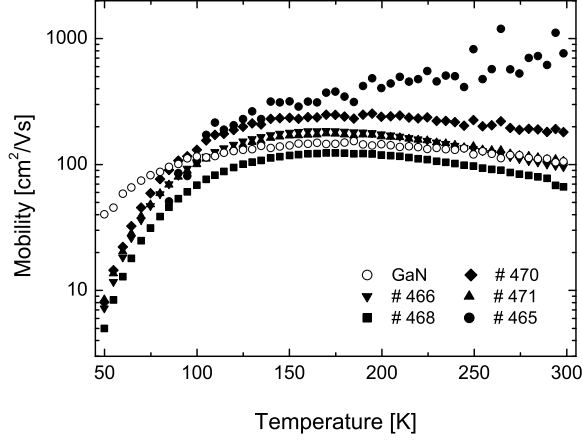


FIG. 12: Electron Hall mobility  $\mu$  as a function of temperature for a GaN layer and a series of (Ga,Fe)N samples with differing Fe content controlled by the  $\text{Cp}_2\text{Fe}$  flow rate.

Figure 13 presents PL spectra acquired in the energy range 2.0 – 3.6 eV at 10 K for two GaN:Fe samples grown with iron precursor flow rates of 50 and 350 sccm. In both samples a weak defect-related yellow luminescence band (YL) centered around 2.2 eV is seen, as well as the excitonic near-band-edge emission. The intensity of the latter is found to increase by four orders of magnitude between the samples with the lowest and the highest Fe content, as shown in Figure 14. The peak position varies between 3.4811 and 3.4833 eV at 10 K, depending on the layer thickness. The determined position and thermal behavior is identical to that of the neutral-donor-bound exciton  $\text{D}^0\text{X}_A$ , related to the upper valence subband of wz-GaN and observed in nominally undoped GaN.<sup>53</sup> However, the peak is noticeably wider, with a FWHM of 4.65 meV for the lowest iron concentration and broadens with increasing doping level.

The lower intensity emission at 3.4609 eV visible in Fig. 15 is assigned to a two electron satellite  $\text{D}^0\text{X}_{A,n=2}$ , where the recombination of the  $\text{D}^0\text{X}_A$  leaves the donor in its excited  $n = 2$  state.<sup>54,55</sup> From the separation between the principal  $\text{D}^0\text{X}_A$  and the  $\text{D}^0\text{X}_{A,n=2}$  maximum, the donor-ionization energy can be obtained.<sup>56</sup> In our case it results in  $E_D \approx 30$  meV, pointing to oxygen or silicon as principal binding site for the  $\text{D}^0\text{X}_A$ . An increase in the oxygen concentration with increasing iron content is confirmed by SIMS data. However, due to the broadening of the excitonic transitions the presence of another donor, with similar binding and ionization energies cannot be ruled out.

Quenching of the excitonic luminescence upon doping with iron is expected, since transition metal impurities in III-V semiconductors are well known to act as carrier lifetime killers.<sup>57</sup> The recovery of the luminescence intensity with increasing iron content appears, therefore, remarkable and cannot be explained by the increase in

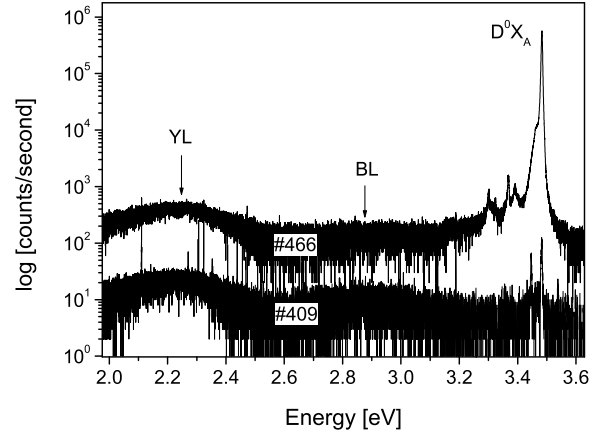


FIG. 13: Photoluminescence spectra at 10 K: comparison between samples with low (#409) and high (#466) Fe concentration.

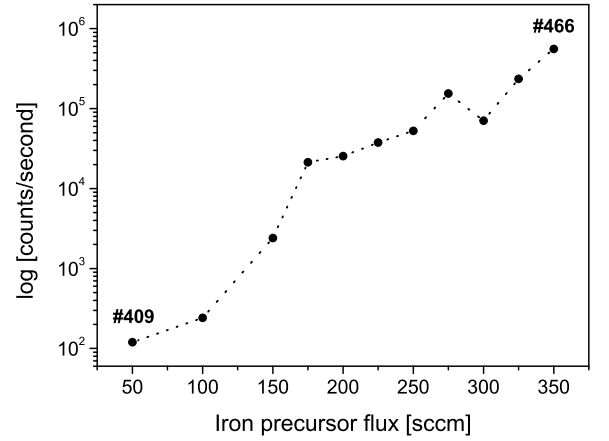


FIG. 14: Near-band-edge emission as a function of the Fe precursor flow rate.

shallow donor concentration alone. Apparently, the neutral donors compete successfully with  $\text{Fe}^{2+}$  in the hole capture. The strong quenching of the excitonic emission observed at low iron contents seems to be predominantly due to the high electron capture rate of  $\text{Fe}^{3+}$ . The change of the charge state of iron with the rise of the electron concentration in our system is, hence, responsible for the recovery of the near band edge emission.

The recombination of electrons and holes on the  $\text{Fe}^{2+/3+}$  acceptor level is accompanied by the characteristic intra-center transition of  $\text{Fe}^{3+}$ . Figures 16 and 17 depict the zero phonon lines of the internal, spin forbidden  ${}^4\text{T}_1(\text{G})\text{-}{}^6\text{A}_1(\text{S})$  transition near 1.3 eV, measured at 20 K under above band-gap excitation in three samples with the same iron content (grown at the lowest iron

precursor flow rate) but different electron concentration. The peaks labelled B, C, D and E at the high energy tail of peak A stem from higher lying levels of the  $^4T_1(G)$  multiplet.<sup>58,59,60</sup>

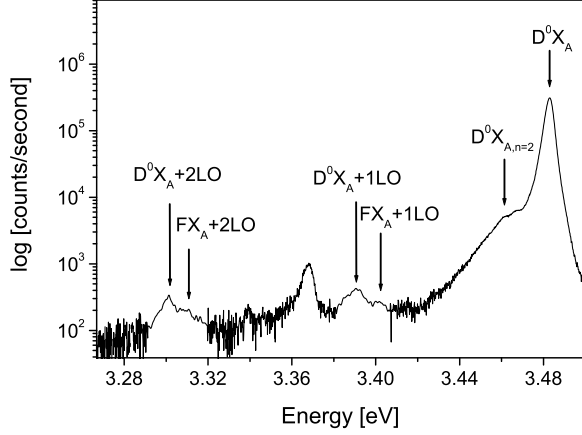


FIG. 15: Near band edge photoluminescence in GaN:Fe. The positions of  $D^0X_A$  and the two electron satellite  $D^0X_{A,n=2}$  are indicated by arrows, as well as those of the LO phonon replicas for the bound- and free-exciton ( $FX_A$ ).

It was found that co-doping with Si (Fig. 17) reduces the intensity of the  $Fe^{3+}$  related emission, while co-doping with Mg (Fig. 16) leads to an intensity enhancement. This behavior is consistent with that of the near band edge luminescence. The increased electron concentration in GaN:Fe,Si as compared to GaN:Fe leads to a reduction of the carrier recombination rate at the  $Fe^{2+/3+}$  acceptor level and, thus, the emission intensity, whereas reduction of the electron concentration (by codoping with Mg) leads to the opposite effect.

#### D. Electron paramagnetic resonance

The samples have also been characterized by electron paramagnetic resonance. The advantage of this technique is that the contributions to magnetization originating from different paramagnetic impurities can be determined separately. It has been found that in all studied structures, independent of the iron concentration, an EPR signal from isolated, substitutional  $Fe^{3+}$  ions is observed. In most samples this signal is superimposed to a strong spectrum stemming from some  $Cr^{3+}$  contamination of the sapphire substrate. In other samples (e.g., #320)  $Er^{3+}$  was observed in the substrate instead of  $Cr^{3+}$ . Typical EPR spectra for the magnetic field oriented along the c-axis are shown in Fig. 18.

The spin Hamiltonian parameters for the  $Fe^{3+}$  ion are determined by a least squares fit of the angular dependence of the EPR line positions for the magnetic field  $\mathbf{B}$  rotated in the (1120) plane - as depicted in Fig. 19

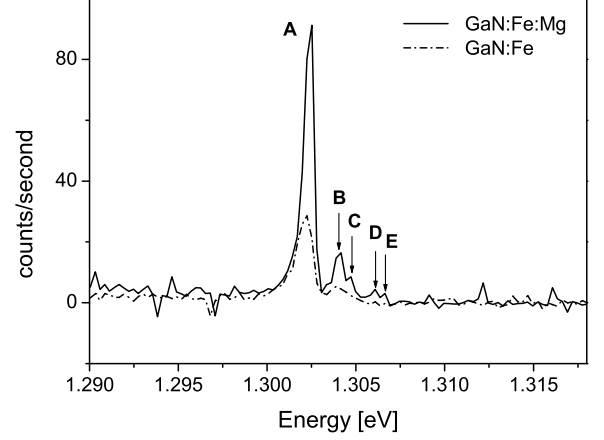


FIG. 16: Intensity dependence of the  $Fe^{3+}$  internal transition as a function of co-doping with Mg.

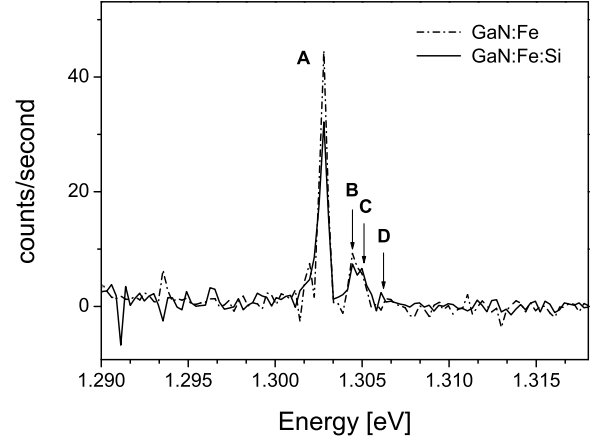


FIG. 17: Intensity dependence of the  $Fe^{3+}$  internal transition as a function of co-doping with Si.

- with the spin Hamiltonian for an  $S = 5/2$  ion in  $C_{3v}$  symmetry:

$$H = \mu_B \mathbf{B} g \mathbf{S} - \frac{2}{3} B_4 (O_4^0 + 20\sqrt{2} O_4^3) + B_2^0 O_2^0 + B_4^0 O_4^0; \quad (8)$$

Here the first and second term describe the Zeeman and the cubic-crystal-field-interaction respectively, and the last two terms represent the second and fourth order trigonal crystal field interactions. The spin Hamiltonian parameters, especially the value of the second order trigonal parameter  $|B_4^0|$ , are found to vary slightly with the sample thickness, giving indication that the layers are strained.

Typical parameters for a  $1 \mu m$  thick layer at moderate Fe precursor flow rates (50 – 200 sccm) are:  $g_{||} = 2.009 \pm$

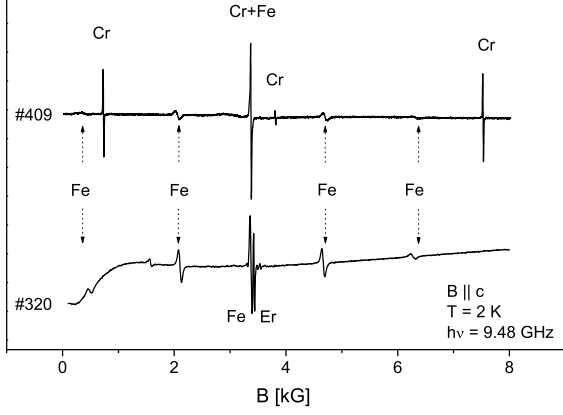


FIG. 18: EPR spectra - first derivative of the microwave absorption with respect to the magnetic field - of  $\text{Fe}^{3+}$  in GaN for the magnetic field direction close to the [0001] GaN axis. The contribution of  $\text{Cr}^{3+}$  and  $\text{Er}^{3+}$  contamination of the sapphire substrate is easily seen. The lower spectrum was taken at a higher microwave power than the upper one (since the EPR signal of  $\text{Er}^{3+}$  is not as easily saturated as that of  $\text{Cr}^{3+}$ ) and a background due to microwave absorption in the cryostat is observed.

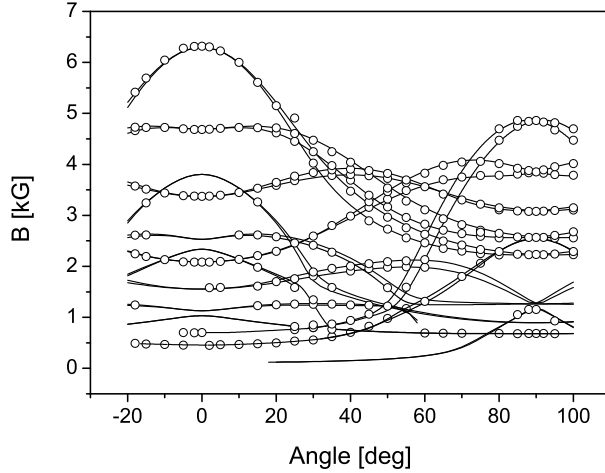


FIG. 19: Angular dependence of the EPR line positions for sample #406. The solid lines represent the fit to experimental data with the Hamiltonian and parameters given in the text.

$0.002$ ,  $g_{\perp} = 2.005 \pm 0.002$ ,  $|B_2^0| = 237.2 \pm 0.6$  G,  $B_4 = 0.11 \pm 0.01$  G, and  $|B_4^0| = 0.8 \pm 0.1$  G.

Figure 20 shows the concentration of  $\text{Fe}^{3+}$  estimated from the EPR signal intensity (circles) compared to the total Fe concentration measured by SIMS (triangles) as a function of the iron source flow rate for two series of samples (full and open symbols). The number of  $\text{Fe}^{3+}$

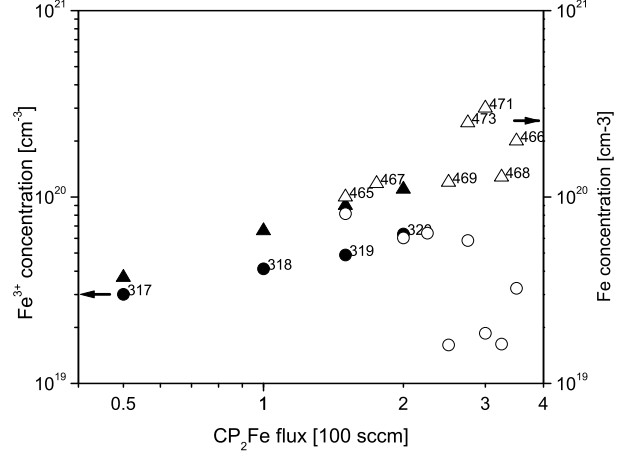


FIG. 20: Concentration of  $\text{Fe}^{3+}$  estimated from the EPR signal intensity (circles) as compared to the total Fe concentration measured by SIMS (triangles) vs. the iron precursor flow rate. Full and open symbols identify two different sample series, grown at the same conditions.

ions in the samples has been determined by comparison with a reference, phosphorus-doped Si sample with a known P concentration of  $2 \times 10^{14} \text{ cm}^{-3}$ . The measurements were performed at low microwave powers in order to ensure that the intensities of both  $\text{Fe}^{3+}$  and P signals were far from the saturation regime. Since the samples could not be measured simultaneously, the relative number of ions is determined with an accuracy of 20%, the uncertainty being due to possible changes in the quality factor of the microwave cavity. Moreover, the relative concentration contains an additional error related to the assumed thickness of the doped layer: the nominal thickness, obtained from the number of observed thickness oscillations in ellipsometry can differ by 20% from the one estimated by SIMS. In the high Fe-doping regime, the accuracy is even lower, since the surface roughness inhibits the observation of the oscillations in ellipsometry as well as a reliable estimation of the thickness from SIMS data. There is also a systematic error related to the estimation of the P content, so that the absolute concentration of  $\text{Fe}^{3+}$  determined from the EPR intensity may differ from the true value by not more than a factor of two. Despite this uncertainty, a clear trend is visible in Fig. 20: with increasing iron precursor flow rate – up to about 200 sccm – the concentration of substitutional  $\text{Fe}^{3+}$  ions increases continuously, but at a lower rate than the total iron concentration in the sample. Above 200 sccm the  $\text{Fe}^{3+}$  content is reduced and considerable fluctuations are observed from sample to sample. We relate this effect to the change of the Fermi level position and, hence, greater occupancy of the  $\text{Fe}^{2+}$  charge state. In the high doping regime a drastic increase of the oxygen donor concentration, by about two orders of magnitude as compared to

that of GaN:Fe grown at low  $\text{Cp}_2\text{Fe}$  flow rates, is detected by SIMS. The oxygen accumulation seems to be correlated with the enhanced sample roughness: as previously underlined, at low flow rates (up to 200 sccm) the GaN:Fe growth is two-dimensional (and the oxygen concentration stays below  $10^{18} \text{ cm}^{-3}$ ), whereas above 200 sccm the (Ga,Fe)N nucleation is granular with over  $1 \mu\text{m}$  fluctuations in the grain height at 350 sccm.

The presence of  $\text{Fe}^{2+}$  ions cannot be determined directly by EPR since the ground state is a spin singlet state and there is no resonance transition observed in the X-band. We have detected a metastable 20% increase of the EPR signal intensity of  $\text{Fe}^{3+}$  under illumination with light of energies above 1.2 eV, confirming the presence of Fe in the 2+ charge state, but no estimations of the actual concentration can be made from such experiments. This increase depends predominantly on the concentration of other, not iron-related trap centers in the sample as well as on the carrier capture rates. Therefore, in order to estimate the total concentration of substitutional Fe ions in the sample, we have analyzed the EPR linewidth of  $\text{Fe}^{3+}$ . The line shape  $A(B)$  of  $\text{Fe}^{3+}$  is found to be excellently described by the derivative of the Gaussian error function:

$$A(B) = \frac{1}{\sqrt{2\pi}\sigma} \exp\left(-\frac{(B - B_0)^2}{2\sigma^2}\right), \quad (9)$$

where  $\sigma^2 = \langle (B - B_0)^2 \rangle$  is the second moment of the distribution. At very low concentrations, the linewidth  $\sigma$  should be mainly governed by interactions with nuclear magnetic moments of the Ga and N isotopes, however, with increasing Fe concentration dipole-dipole interactions between iron ions should lead to line broadening. The broadening due to dipole-dipole interaction consists of two contributions: one due to the interaction with other 3+ ions and one related to the interaction with Fe ions in the 2+ charge state. This is true as long as the Fermi level is pinned to the  $\text{Fe}^{2+/3+}$  acceptor level and the oxygen ions have no magnetic moment, which seems to be justified, since no EPR transition related to O donors is observed. Both contributions depend on the  $i^{\text{th}}$  to  $j^{\text{th}}$  ion distance  $r_{ij}$ , as  $r_{ij}^{-3}$ . Assuming that the ions as well as their charges are uniformly distributed in the lattice, one can expect a linear correspondence between the dipolar broadening  $\sigma - \sigma_0$  and the Fe concentration. Figure 21 gives the linewidth as a function of iron precursor flow rate for the  $-1/2 \rightarrow 1/2$  transition of  $\text{Fe}^{3+}$  at  $\mathbf{B} \parallel [0001]$  for the same samples shown already in Fig. 20.

As it can be seen, the linewidth increases continuously with the  $\text{Cp}_2\text{Fe}$  flow rate up to 250 sccm and saturates above this value. By taking  $\sigma_0 = 12 \text{ G}$  for the unbroadened linewidth we obtain, in the low doping regime, exactly the same slope for the dipolar line broadening versus  $\text{Cp}_2\text{Fe}$  flow rate as that for the SIMS concentration in Fig. 20. This allows us to set the solubility limit for substitutional iron in GaN at our growth conditions (that is, the saturation concentration obtained from the EPR

linewidth) to  $1.8 \times 10^{20} \text{ cm}^{-3}$ , *i.e.*, 0.4%. It should be noted that in contrast to concentration estimations from the EPR signal intensity, in the case of EPR linewidth there is no error related to the determination of the sample thickness, therefore the comparison with SIMS data is more straightforward.

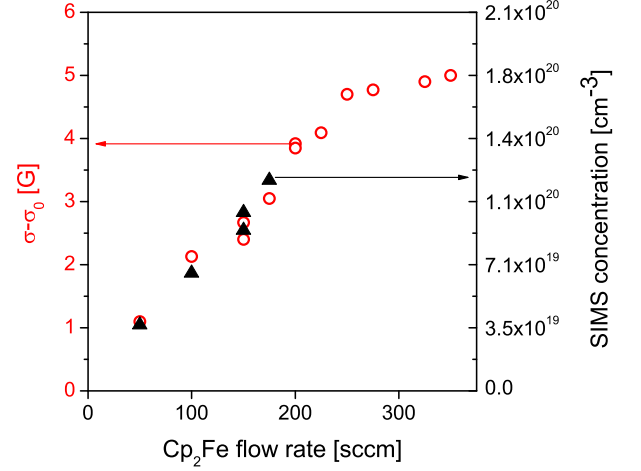


FIG. 21: EPR linebroadening (left y-axis) as a function of the iron precursor flow rate (hollow circles) for  $\sigma_0 = 12 \text{ G}$ . The SIMS concentration (right y-axis) at low flow rates, denoted by full triangles, is shown for comparison.

The relatively narrow linewidth in the high doping regime visible in Fig. 21 indicates that the substitutional Fe ions remain well isolated and interact only very weakly *via* dipole-dipole interaction. This is consistent with the TEM data, revealing the presence of iron-rich nanocrystals in which excess iron is accumulated. These nanocrystals do not contribute to the  $\text{Fe}^{3+}$  EPR. As we already underlined, the nanocrystals are located in the upper half of the (Ga,Fe)N layer towards the surface and may deplete this part of the layer from isolated Fe ions which thus remain in the lower region of the layer only. It is worth also noting that the coexistence of  $\text{Fe}^{3+}$  and  $\text{Fe}^{2+}$  ions implied by the EPR data as well as by the SQUID results, suggests that the Fermi level is pinned well below the conduction band minimum by the  $\text{Fe}^{3+}/\text{Fe}^{2+}$  acceptor states. Such pinning is in contradiction with the relatively high value of electron concentration and mobility we observe in this high  $\text{Cp}_2\text{Fe}$  flux range, as shown in Figs. 10 and 12, giving clear indication that the Fermi level is located either in the conduction band or in the donor impurity band. The simultaneous observation of  $\text{Fe}^{3+}$  ions (as evidenced by EPR) and free electrons (as shown by the Hall data) in the high Fe concentration regime is one of the surprising findings of the present work. In view of our TEM data, it is natural to suggest that the conduction proceeds *via* the upper region of the layer depleted from isolated Fe acceptors, while  $\text{Fe}^{3+}$  ions

exist mainly in the part of the layer closer to the interface with the GaN buffer.

## E. Magnetic properties of (Ga,Fe)N

### 1. Paramagnetic contributions

Figure 22 gives the temperature dependence of the magnetic susceptibility  $\chi(T)$  obtained from SQUID magnetization measurements at a constant magnetic field of 0.1 T for four GaN:Fe samples with a low Fe content. As it can be seen, two components of  $\chi(T)$  may be distinguished: one is a Curie-type of paramagnetism  $\chi(T) \sim 1/T$ , which we assign to  $\text{Fe}^{3+}(\text{d}^5)$  ions. The concentration of  $\text{Fe}^{3+}$  ions obtained under this assumption is shown in Table I for the samples under investigation. The second component is a temperature independent contribution dominating at high temperatures. However, as shown in Fig. 23, the magnetization at high temperature in addition to the paramagnetic part linear in the magnetic field, contains a ferromagnetic component. Properties and origin of the high temperature ferromagnetism in (Ga,Fe)N will be discussed later.

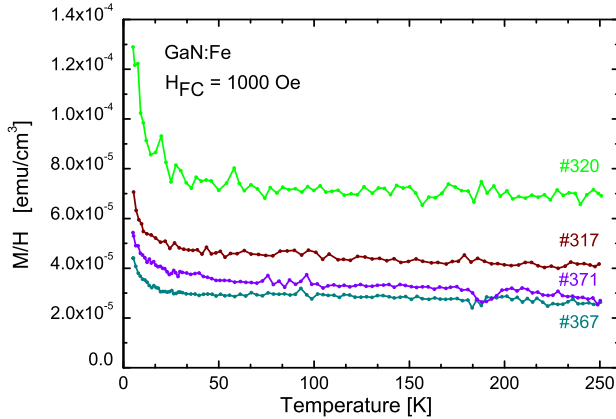


FIG. 22: Magnetic susceptibility as a function of temperature, showing the temperature independent and the temperature dependent components assigned to the Van Vleck and Curie paramagnetism, respectively. The ferromagnetic and substrate contributions (temperature independent and linear in the field) have been subtracted.

We attribute the term linear in the magnetic field to Van Vleck paramagnetism, most likely originating from the Fe ions in the  $2+(\text{d}^6)$  charge state. The presence of Fe ions in such a charge state seems to correlate with the Hall effect measurements which, according to Fig. 11, indicate that the Fermi level for low Fe flow rates may be pinned to the  $\text{Fe}^{3+/2+}$  level. The coexistence of Fe in the  $3+$  and  $2+$  charge states is also confirmed by photo-EPR results and the theoretical explanation of the Van Vleck

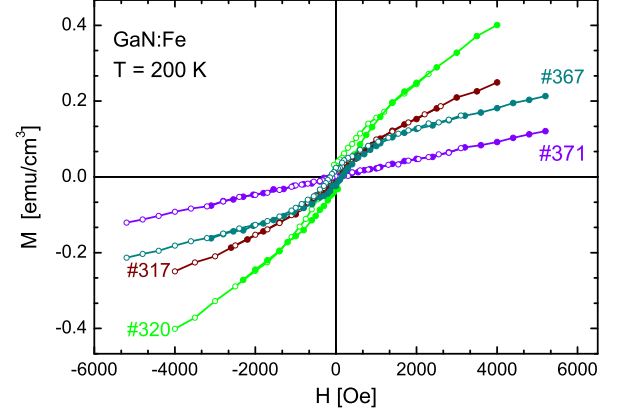


FIG. 23: Magnetization from SQUID measurements at 200 K for a series of (Ga,Fe)N samples with different Fe content (solid symbols). The substrate contribution (temperature independent and linear in the field) has been subtracted in this and in the figures that follow. Data obtained by numerical reflection, if only a half of the hysteresis cycle has been measured, are shown by open symbols.

contribution is currently being formulated.<sup>61</sup>

### 2. Ferromagnetic properties

Ferromagnetic signatures, such as magnetic hysteresis, remanent magnetization ( $M_{\text{rem}}$ ), and coercivity ( $H_c$ ) are detectable in all our Fe-doped films but with the increase of the total Fe concentration above the solubility limit of 0.4% the ferromagnetic component exceeds the paramagnetic contributions previously discussed. This is depicted in Fig. 24, which shows the magnetization cycles at 5 K for samples with various Fe contents. A rather clear ferromagnetic component is seen, with its strength increasing upon the increase of the Fe content. For the layers with the highest Fe concentration, we recover about 25% of the Fe ions contributing to the saturation value of magnetization, if  $S = 2$  and  $g = 2$  are assumed.

According to the findings summarized in Fig. 25, the ferromagnetic signal does not diminish remarkably when the temperature is increased to 200 K, and it persists up to above room temperature, as shown in the inset. The set of magnetization curves obtained in the full available temperature and field range allows to establish the temperature variation of spontaneous magnetization  $M_S$ , determined from the Arrot plot, as depicted in Fig. 26. If the ideal Brillouin  $M_S(T)$  dependence is assumed, the data displayed in the inset point to an apparent Curie temperature  $T_C$  of  $\sim 500$  K. The ferromagnetism in question reveals a well defined anisotropy. Figure 27 shows that the saturation value of magnetization is greater for the magnetic field perpendicular to the wurzite  $c$ -axis. Interestingly, a similar anisotropy was observed in the

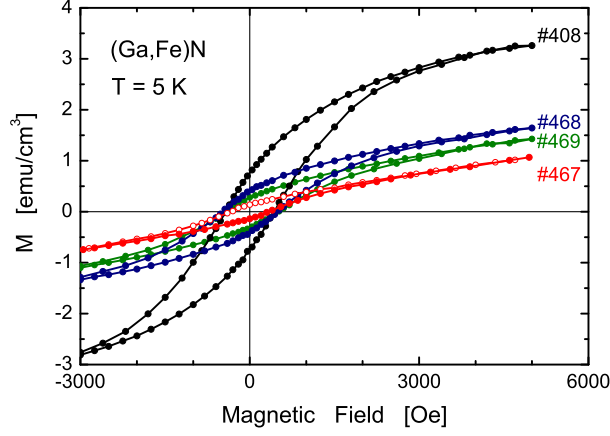


FIG. 24: Magnetization at 5 K for a series of (Ga,Fe)N samples with various Fe contents (solid symbols). Data obtained by numerical reflection, if only a half of the hysteresis cycle has been measured, are shown by open symbols.

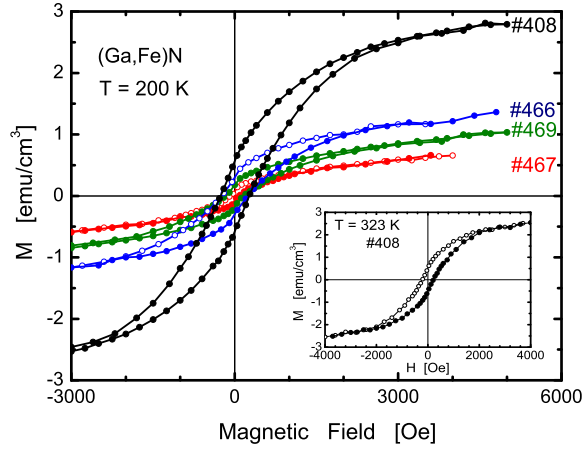


FIG. 25: Magnetization at 200 K for a series of (Ga,Fe)N samples with various Fe content (solid symbols). Inset: above room temperature  $M(H)$  for sample #408. Data obtained by numerical reflection, if only a half of the hysteresis cycle has been measured, are shown by open symbols.

case of (Zn,Co)O.<sup>62</sup>

We want to underline here that we do not take all the above ferromagnetic signatures as a solid proof of a uniform ferromagnetic state of (Ga,Fe)N. In the material under consideration here, the average concentration of magnetic ions is far below the percolation limit for the nearest-neighbor coupling, and at the same time the free-carrier density is too low to mediate an efficient long-range exchange interaction. Hence, we take the presence of high temperature ferromagnetism as an indication of the non-uniform distribution of the Fe ions over the GaN

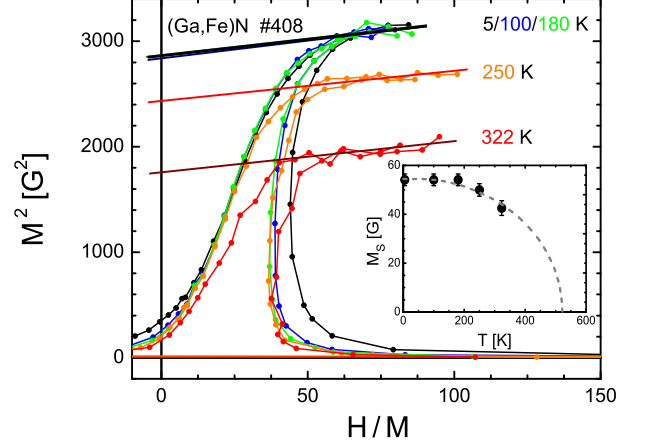


FIG. 26: Determination of the spontaneous magnetization at various temperatures obtained by plotting the square of the magnetization vs. the ratio of the magnetic field to the magnetization (Arrot plot, sample #408). The inset shows the established spontaneous magnetization as a function of temperature, whose extrapolation leads to the apparent Curie temperature of 500 K for the same sample.

lattice already demonstrated *via* TEM analysis of the structures.

In order to shed some light on the origin of the ferromagnetic behavior presented in the last figures, we discuss at first the results from zero-field cooled (ZFC) and field cooled (FC) magnetization measurements at a low magnetic field of 50 Oe, given in Fig. 28. The markedly different behavior, namely the increasing FC-ZFC difference on lowering temperature, is indicative of the fact that the sample is in a magnetically frozen state having its response determined by thermally activated processes across some energy barriers. We further note that the ZFC and the FC magnetizations are characterized by temperature gradients of opposite sign without a maximum appearing in the ZFC curve. Such a behavior can be expected for an ensemble of magnetically anisotropic ferromagnetic particles thermally cycled below its blocking temperature ( $T_B$ ). At  $T < T_B$  the moments of some of the particles are blocked and unable to surmount the magnetic energy barriers at the time scale of the experiment. The energy barriers in the vicinity of  $H = 0$ , cannot be overcome without an increase in the thermal energy (or an external magnetic field). For a system of non-interacting, uniaxial particles the energy barrier for the magnetization reversal is  $\Delta E = KV$ , where  $V$  is the particle volume and  $K$  is the anisotropy energy density. Therefore, the actual magnetic behavior depends on the measuring time ( $t_m$ ) of the specific experimental technique with respect to the time  $t$  required to overcome the energy barrier (for DC magnetic studies a  $t_m$  of 100 s is usually adopted). Accordingly, for a system of

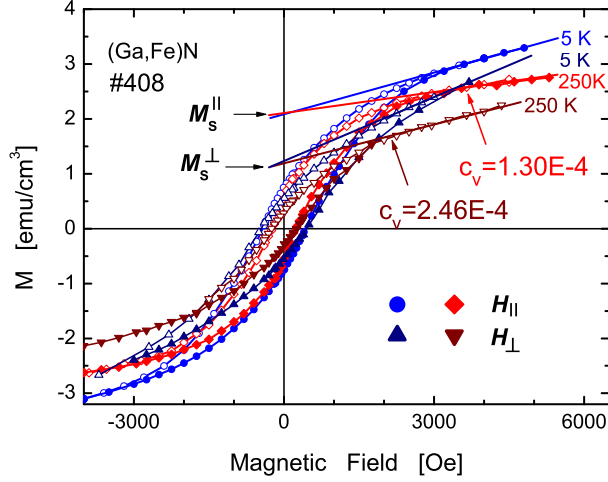


FIG. 27: Magnetization measurements for sample #408 (solid symbols), indicating that the saturation value of magnetization is greater for the magnetic field  $H_{||}$  along the surface of the sample (perpendicular to the  $c$ -axis). Data obtained by numerical reflection, if only a half of the hysteresis cycle has been measured, are shown by open symbols.

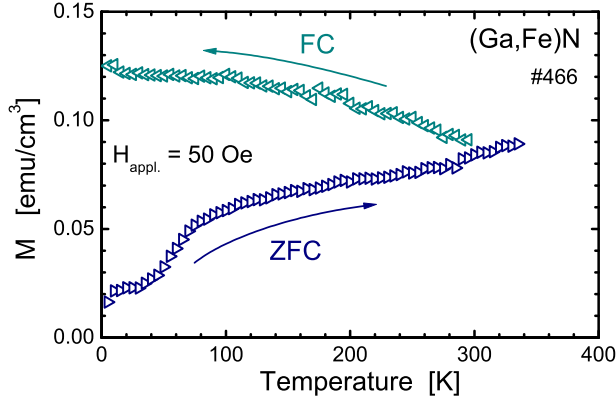


FIG. 28: Magnetization of sample #466 measured at  $H_{appl.} = 50$  Oe after cooling the sample in absence of the external field (ZFC) and during cooling in the same  $H_{appl.}$ . Qualitatively the same results are obtained at  $H_{appl.} = 200$  Oe.

identical non-interacting uniaxial particles, the following simple condition for the evaluation of  $T_B$  is employed:

$$T_B \simeq KV/25k_B. \quad (10)$$

Therefore,  $T > T_B$  defines the onset of superparamagnetic behavior for this system, whereas below  $T_B$  an irreversible behavior is expected. Within this line of interpretation, our experiment (Figs. 23-28) points then to a large, at least above room temperature  $T_B$  for (Ga,Fe)N layers.

This is a rather high value and it indicates that the ferromagnetic particles in (Ga,Fe)N contributing to the ferromagnetic response must be characterized by substantial values of the  $KV$  product. The existence of fine entities in the studied samples is corroborated by our TEM analysis, revealing the presence of wurzite nanocrystals embedded in the host GaN. The substantial amount of these nanocrystals, as measured by the value of  $M_S$ , is clearly triggered by higher flow rates (above  $\sim 150$  sccm) – see Fig. 29 – and undoubtedly correlates with the nominal Fe concentration in the layers. Furthermore, as already pointed out, EDS results demonstrate that the Fe concentration is largely enhanced within the nanocrystals.

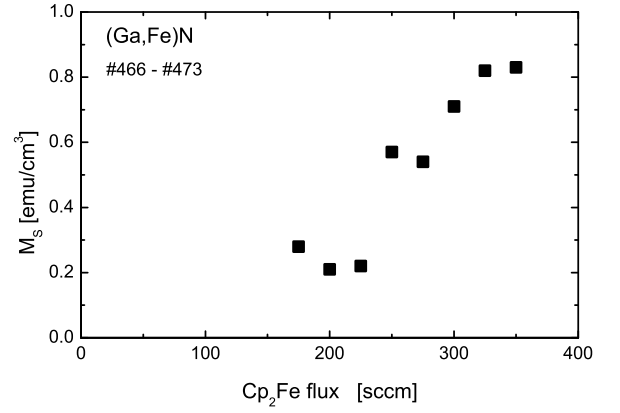


FIG. 29: Saturation magnetization of the ferromagnetic component extracted from  $M(H)$  curves at 200 K for the #466 - #473 layer series versus the Fe precursor flow rate.

All these findings imply that in the case of Fe contents above the solubility limit (Ga,Fe)N undergoes a spinodal decomposition into regions with small and large concentrations of magnetic ions, so that most of Fe ions resides in the magnetic nanocrystals. Now, taking the volume of these Fe-rich nanocrystals as  $V = 1000 \text{ nm}^3$  on average, we end up with a requirement for  $K$  to be  $\simeq 20 \times 10^5 \text{ erg/cm}^3$  to reproduce a  $T_B$  of about 500 K, as the magnetization studies indicate. This value is four times higher than that of bulk cubic iron and it is a half of that of hexagonal cobalt. However, the estimated large value for  $K$  should be treated rather as an upper limit, since  $T_B$  can get enlarged above the value predicted by Eq. 10 if, as a result of the magnetic interaction between particles, an ordering of the magnetic moments takes place. Moreover, we note that the nanocrystals are not monodispersed and that the distribution in their volumes gives rise to a distribution in the blocking temperatures. Thus, Eq. 10 gives the mean  $T_B$  for the system, so that irreversible effects occur also above  $T_B$  and, therefore, the requirements for the magnitude of  $K$  are considerably relaxed.

## V. SUMMARY AND OUTLOOK

Our results on the GaN:Fe and (Ga,Fe)N systems have reemphasized the importance of two related and generic aspects of magnetically doped wide band-gap semiconductors. First, most of the substitutional magnetic impurities give rise to the presence of deep levels originating from open  $d$  or  $f$  shells of the impurity atoms. The presence of such levels strongly affects the electrical and the optical properties of these materials systems. At the same time, co-doping with shallow impurities, by changing the charge and, thus, the spin state of the magnetic ions, can serve to alter the magnetic response. Second, though depending on the growth conditions, the TM solubility limit is rather low and typically – except for Mn – it is hard to introduce more than 1% of magnetic impurities into randomly distributed substitutional sites. Due to the low density and in absence of band carriers, the impurity spins can be regarded as decoupled. Accordingly, pertinent properties of the system can be adequately described by the single-impurity theory.<sup>63</sup> The series of transport, optical, EPR, and magnetic experiments that we have reported here for MOCVD grown (Ga,Fe)N and for (Ga,Fe)N co-doped with either Si or Mg has substantiated the notion that the material characteristics are determined by the  $\text{Fe}^{3+}/\text{Fe}^{2+}$  acceptor-like deep level. Thus, the relative concentrations of  $\text{Fe}^{3+}$  and  $\text{Fe}^{2+}$  ions and, hence, the relative importance of the Curie and Van Vleck paramagnetism is defined by the density of shallow acceptors and donors. This means, in particular, that if the acceptor concentration were high enough to give rise to the presence of a sufficiently increased density of weakly localized or delocalized valence band holes, the carrier-mediated coupling between spins localized on  $\text{Fe}^{3+}$  ions would operate.<sup>6</sup> Our experiments have indicated also that the solubility limit is about 0.4% in the case of Fe in GaN under our growth conditions.

A number of scenarios can be realized when increasing the Fe concentration beyond the solubility limit. One would be the appearance of Fe in interstitial positions, where it will act as a double donor. We have indeed found a strong increase in the electron concentration in this regime. EXAFS or Rutherford backscattering experiments might allow to detect the presence of interstitial Fe. A further scenario is represented by the crystallographic phase separation in the form of precipitates of Fe or Fe-compounds. Finally, an appealing possibility is the existence of spinodal decomposition into regions with respectively high and low concentrations of the magnetic constituent. Our TEM results have demonstrated the presence of coherent Fe-rich nanocrystals embedded and stabilized by the GaN host. Furthermore, the TEM imaging shows that these nanocrystals are not distributed uniformly over the layer but float towards the surface during the growth process. The resulting inhomogeneity in the layer structure along the growth direction may account for the increased surface roughness at high doping level, as observed by AFM. This inhomogeneity may also give

reason for the simultaneous presence of deep Fe acceptors and conducting electrons demonstrated by our transport, EPR, and SQUID experiments. We argue that the Fe-rich nanocrystals account for the high-temperature ferromagnetic properties of the (Ga,Fe)N films grown by MOCVD and MBE as well as of GaN implanted with Fe. We note that the GaN host may stabilize nanocrystals of a composition and structure non-existing in the case of a free standing Ga-Fe-N material systems. Actually, such a situation has lately been found in the case of MBE grown (Ge,Mn), where spinodal decomposition into Ge and novel Mn-rich (Ge,Mn) nanowires has been revealed.<sup>40</sup> Furthermore, it has recently been suggested by one of us<sup>64</sup> that the aggregation of magnetic nanocrystals can be modified by altering the charge state of magnetic impurities during the growth or by thermal treatment during or upon deposition. This can obviously be accomplished by co-doping with shallow donors and acceptors. Experiments in this direction are on the way. While our paper is concerned with one material system, namely GaN:Fe – (Ga,Fe)N, there is ground to conjecture that spinodal decomposition and inhomogeneity along the growth direction revealed by our work, as well their influence on transport, optical, and magnetic characteristics, are generic properties of diluted magnetic semiconductors and diluted magnetic oxides showing high apparent Curie temperatures. Within this model, the spontaneous magnetization originates from magnetic moments of ferromagnetic or ferrimagnetic nanoclusters or from uncompensated spins at the surface of antiferromagnetic nanoparticles. We are confident that the identification of the actual chemical nature of nanocrystals in particular matrices and the determination of the mechanisms accounting for the elevated blocking temperatures necessary to make the ferromagnetic-like characteristics to survive up to high temperatures, will attract considerable attention in the years to come.

## Acknowledgments

This work was partly supported by the Austrian Fonds zur Förderung der wissenschaftlichen Forschung - FWF (projects FWF-P17169-N08 and FWF-N107-NAN) and by the EC project NANOSPIN (FP6-2002-IST-015728). The set-up for *in-situ* XRD has been provided by PANalytical B.V., Almelo, The Netherlands. We are grateful to O. Fuchs for his precious technical support.

## Appendix: Experimental difficulties and precautions in SQUID measurements

*General remarks* – the (Ga,Fe)N layers are grown on 330  $\mu\text{m}$  thick sapphire substrates, so they constitute only a fraction of the whole volume of the investigated material, and their magnetic moment is very-small to small when compared to the diamagnetic signal of the sub-

strate. Since it is unfeasible to remove the sapphire substrate, the magnetic moment of the (Ga,Fe)N system has to be established by post-measurement subtraction of the known magnetic moment of a Fe-free, but otherwise identical GaN/sapphire reference sample. This in general does not pose any experimental difficulties if the signal to be investigated is at least comparable to the substrate signal. In the case of our epitaxial layers of magnetically diluted materials, the weak magnetic response, as shown later, requires typically more than 90% compensation, approaching 99% for the lowest Fe concentration. Furthermore, the overall measured signals are rather weak, so there is little room left for a significant improvement of the absolute accuracy of the experimental data after the compensation, as we are approaching the base noise level of the magnetometer set up. Results of typical measurements are depicted in Fig. 30, exemplifying the necessity for high quality, distortion free measurements. Additionally, any experimental flaws, short-cut

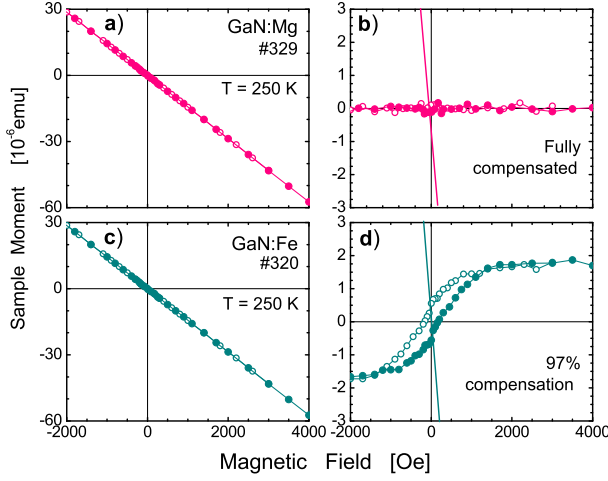


FIG. 30: Typical examples of magnetic moment vs. magnetic field  $m(H)$  recorded for the layers presented in this paper. Left panels: raw data. Right panels: after subtracting the major linear component. The high slope lines on the left panels indicate the uncompensated  $m(H)$  data. Data obtained by numerical reflection, if only a half of the hysteresis cycle has been measured, are shown by open symbols.

procedures or negligences in the sample handling have severe adverse effects on the reliability of the final results, as they get strongly magnified by the high degree of compensation analysis required to determine the signal from these layers. To preserve the credibility of the measurement, tight constraints on the whole measurement process are imposed and can be generalized as: contamination-free handling of the samples, magnetically-clean mounting in the SQUID magnetometer, and credibility in the determination of the magnetic moment by the magnetometer software.

*a. Handling of the samples* We perform all the manual operations, including the sample mounting on the magnetometer sample holder, in a laminar flow cabinet equipped with an absolute filter. Also, we avoid to bring the samples into contact with any ferrous materials, including metal tweezers,<sup>65</sup> since (stainless) steel tweezers are a well recognized source of contamination<sup>66</sup> of, *e.g.*, silicon wafers and their magnetic signature can be comparable with the magnetic response expected in our studies.<sup>65</sup> However, contrary to Si, where the contamination can occur either by contact chemical reaction or by mechanical scratching, we believe that in our case mostly a mechanical grinding of the softer metal by the much harder sapphire/GaN is the major source of magnetic contamination. Therefore, we employ only titanium-/plastic-based tweezers. Another potential source of specimen contamination is related to the dicing of the sapphire wafer, as it requires a diamond saw. For the preparation of our samples, we employ only plastic-based cutting wheels on the wafer coated with photoresist for additional protection. After dicing, the samples are rinsed with organic solvents in an ultrasonic cleaner. We verified that none of these substances carries any detectable amounts of ferrous metals.

*b. Sample holder and sample mounting* In the present study we utilize a home-made SQUID magnetometer built into a standard cryostat operating from 5 to 325 K in continuous flow mode. Although equipped with a 1 T superconducting coil, the set-up has been optimized for very weak field operation and the noise level, increasing with the field, limits our experimental abilities to  $\sim 0.5$  T. We use a commercially available SQUID sensor and the matched electronics, connected to a computer based acquisition system running under an home developed code. The sensing end of the set-up, like most modern similar systems, utilizes the controlled tripping of the sample (with the sample holder) through sensing coils arranged in the 2nd order gradiometer configuration. Ideally, only the sample to be measured produces the signal. Its position-related voltages generated by the SQUID electronics during this movement form the base for the numerical procedures necessary for extraction of the magnetic moment. In general, a gradiometer configuration allows the use of any uniform extended object – rod-like shaped – as a sample holder, since if its length is much larger than the extent of the pick-up coils, the sample holder produces no output according to symmetry considerations. In reality, the limited length of the sample chamber does not allow sufficiently long sample holders, resulting in a non-linear position-dependent voltage disturbing the signal from the sample, particularly in the most sensitive ranges. This parasitic contribution can be largely reduced by employing magnetically weak substances, preferably diamagnets, shaped in the form of small tubes or rods. Nothing, however, will compensate for the shape variations and for the distribution of inhomogeneous magnetic impurity inside the rod material. The former result from all sort of mechanical imperfec-

tions (e.g. variable cross section area, scratches, etc.), the latter may be an inherent property of the chosen material. Both generate position-dependent voltages that modulate or distort the signal from the sample in an unknown and a-priori unpredictable  $T$ - and  $H$ - dependent way, corrupting, in this way, the results of the measurements in an unrecoverable way. Therefore, the testing of the sample holder and the selection against the parasitic magnetic signal turns out to be of a great importance for this study.

Currently, the most popular choice for magnetometer sample holders are drinking straws, not only because of their low magnetic signature, but also due to the flexibility allowed in a glue-free mounting of samples with dimensions comparable with the diameter of the straw. For the purposes of our studies, we have undertaken an accurate testing of the available materials, focusing in particular on those directly provided by Quantum Design.<sup>67</sup> Some 30 straws were scanned along their length at 3000, 1000 Oe, and at remanence, usually at low  $T$  (10 K), and occasionally at 200 K. All tested straws have been thoroughly cleaned in organic solvent prior to the tests. The collected position dependent signals are processed according to the same numerical steps employed to establish the magnetic moment in the magnetometer, so that the spatial distribution of the magnetic moment along the straws could be established. We have found that although on average the straws have a small magnetic signature suitable for general magnetic investigations (exhibiting moment variations below  $2 \times 10^{-7}$  emu on a one inch span near their central part), only two went below  $\sim 5 \times 10^{-8}$  emu, reaching in this way the upper limit required for our studies. Instead of using potentially problematic straws, we opted for  $\sim 20$  cm long and 1 or 2 mm wide Si strips cut from 8" commercial wafers.<sup>68</sup> After a thorough testing, we have found that all the strips conform to our stringent requirements concerning the magnetic uniformity. Additionally, the Si strips ensure an excellent rigidity and allow for an easy sample mounting in various in-plane orientations. The major drawback of switching to Si strips is the necessity of using a glue to fix the sample onto the strip. After testing many substances for a possible contribution to the measurement as well as for mechanical reliability and low temperature behavior we settled for the heavily diluted GE varnish, which best

fulfills all requirements. We found that only the recently available orange version,<sup>69</sup> as opposed to the dark red one, shows no magnetic signature down to 5 K and up to 3000 Oe even when examining  $\sim 10$  times the amount normally needed for mounting. It must be noted, that the usage of narrow strips may lead to larger sample off centering than in the case of wider straws. In our case however, owing to the relatively large diameter of our pick-up coils we determined this effect to be below 0.5%,<sup>70</sup> i.e. within the typical run-to-run non-reproducibility of our system.

*c. Reduction of the data* Typically the investigated magnetic moment is established by a numerical fitting (least square regression) of an ideal, point dipole response function of the gradiometer pickup coils into the set of voltages collected during the tripping of the sample through the coils. In the case of macroscopically large samples of rectangular shape the form of the real response function starts to differ noticeably if the specimens occupy more than a few percent of the volume of the pickup coils.<sup>71</sup> As a consequence, even the best possible fitting routine will not establish the accurate sample moment, unless the response function gets adequately modified. It is relatively easy to extend the point dipole response function to account for uniformly magnetized body of a given length<sup>70,71,72</sup> and this length parameterized function is routinely used in our system to extract a length-independent magnetic moment. This however seems to be the only one feasible to compensate sample size effects. The account of other detrimental effects like non uniform sample extension in the plane perpendicular to the magnetometer axis or displacement of the whole sample aside from the axis is too complex to get generalized in any sort of universally parameterized function. So, in order to minimize their adverse influence on the experimental results, we confined ourselves to one sample size for magnetic measurement and additional care is taken to mount the samples on Si sticks in a reproducible way. For completeness, we note that from the results of numerical modelling<sup>70,71</sup> a maximum 1% of moment distortion is expected for the samples used in the experiment. Therefore, we can safely conclude that although potentially large, the sample-size-related effects should not systematically alter the magnetometer results before and after the compensation.

<sup>1</sup> T. Dietl and H. Ohno, MRS Bulletin p. 714 (2003).

<sup>2</sup> S. J. Pearton, C. R. Abernathy, M. E. Overberg, G. T. Thaler, D. P. Norton, N. Theodoropoulou, A. F. Hebard, Y. D. Park, F. Ren, J. Kim, et al., J. Appl. Phys. **93**, 1 (2003).

<sup>3</sup> W. Prellier, A. Fouchet, and B. Mercey, J. Phys.: Condens. Matter **15**, R1583 (2003).

<sup>4</sup> T. Dietl, in *Proceedings 27th International Conference on the Physics of Semiconductors, Flagstaff, USA, 2004*, edited by C. G. V. d. W. J. Menéndez (AIP, Melville,

2005), p. 56.

<sup>5</sup> C. Liu, F. Yun, and H. Morkoç, J. Materials Science: Materials in Electronics **16**, 555 (2005).

<sup>6</sup> T. Graf, S. T. B. Goennenwein, and M. S. Brandt, Phys. Status Solidi **B 239**, 277 (2003).

<sup>7</sup> T. Dietl, in *Materials Research Society Fall Meeting, Boston, USA, Nov. 2004, MRS Proceedings*, edited by C. Wetzel, B. Gil, M. Kuzuhara, and M. Manfra (2004), vol. 831.

<sup>8</sup> F. Matsukura, H. Ohno, and T. Dietl, in *Handbook of Mag-*

- netic Materials*, edited by K. Buschow (Elsevier, Amsterdam, 2002), vol. 14, p. 1.
- <sup>9</sup> S. A. Wolf, D. D. Awschalom, R. A. Buhrman, J. M. Daughton, S. von Molnár, M. L. Roukes, A. Y. Chtchelkanova, and D. M. Treger, *Science* **294**, 1488 (2001).
  - <sup>10</sup> S. Pearton, M. Overberg, G. Thaler, C. Abernathy, N. Theodoropoulou, A. Hebard, S. Chu, R. Wilson, J. Zavada, A. Polyakov, et al., *J. Vac. Sci. Technol. A* **20**, 721 (2002).
  - <sup>11</sup> N. Theodoropoulou, A. Hebard, S. Chu, M. Overberg, C. Abernathy, S. Pearton, R. Wilson, and J. Zavada, *J. Appl. Phys.* **91**, 7499 (2002).
  - <sup>12</sup> Y. Shon, Y. H. Kwon, Y. Park, S. Yuldashev, S. J. Lee, C. Park, K. Chung, S. Yoon, H. Kim, W. Lee, et al., *J. Appl. Phys.* **95**, 761 (2004).
  - <sup>13</sup> U. Wahl, A. Vantomme, G. Langousche, J. G. Correia, L. Peralta, and T. I. Collaboration, *Appl. Phys. Lett.* **78**, 3217 (2001).
  - <sup>14</sup> H. Akinaga, S. Nemeth, J. D. Boeck, L. Nistor, H. Bender, G. Borghs, H. Ofuchi, and M. Oshima, *Appl. Phys. Lett.* **26**, 4377 (2000).
  - <sup>15</sup> S. Kuwabara, K. Ishii, S. Haneda, T. Kondo, and H. Munekata, *Physica E* **10**, 233 (2001).
  - <sup>16</sup> S. Kuwabara, T. Kondo, T. Chikyow, P. Ahmet, and H. Munekata, *Jpn. J. Appl. Phys.* **40**, L727 (2001).
  - <sup>17</sup> H. Ofuchi, M. Oshima, M. Tabuchi, Y. Takeda, H. Akinaga, Š. Németh, J. D. Boeck, and G. Borghs, *Appl. Phys. Lett.* **78**, 2470 (2001).
  - <sup>18</sup> S. Heikman, S. Keller, T. Mates, S. DenBaars, and U. Mishra, *J. Cryst. Growth* **248**, 513 (2003).
  - <sup>19</sup> M. Kane, S. Gupta, W.E.Fenwick, N. Li, E.H.Park, M. Strassburg, and I. Ferguson, *Phys. Stat. Sol. (b)* (in print).
  - <sup>20</sup> H. Przybylińska, A. Bonanni, A. Wolos, M. Kiecana, M. Sawicki, T. Dietl, H. Malissa, C. Simbrunner, M. Wegscheider, H. Sitter, et al., *Materials Science and Engineering B* **126**, 222 (2006).
  - <sup>21</sup> A. Bonanni, C. Simbrunner, M. Wegscheider, H. Przybylińska, A. Wolos, H. Sitter, and W. Jantsch, *phys. stat. sol. (b)* **243**, 1704 (2006).
  - <sup>22</sup> K. Sato and H. Katayama-Yoshida, *Semicond. Sci. Technol.* **17**, 367 (2002).
  - <sup>23</sup> S. Mirbt, B. Sanyal, and P. Mohn, *J. Phys.: Condens. Matter* **14**, 3295 (2002).
  - <sup>24</sup> B. Sanyal, O. Bengone, and S. Mirbt, *Phys. Rev. B* **68**, 205210 (2003).
  - <sup>25</sup> X. Cui, B. Delley, A. Freeman, and C. Stampfl, *Phys. Rev. Lett.* **97**, 016402 (2006).
  - <sup>26</sup> K. Maier, M. Kunzer, U. Kaufmann, J. Schneider, B. Monemar, I. Akasaki, and H. Amano, *Mater. Sci. Forum.* **143 - 147**, 93 (1994).
  - <sup>27</sup> J. Baur, K. Maier, M. Kunzer, U. Kaufmann, and J. Schneider, *Appl. Phys. Lett.* **65**, 2211 (1994).
  - <sup>28</sup> E. Malguth, A. Hoffmann, W. Gehlhoff, O. Gelhausen, M. R. Phillips, and X. Xu, *Phys. Rev. B* **74**, 165202 (2006).
  - <sup>29</sup> A. Bonanni, D. Stifter, A. Montaigne-Ramil, K. Schmidegg, K. Hingerl, and H. Sitter, *J. Cryst. Growth* **248**, 211 (2001).
  - <sup>30</sup> S. Heikmann, S. Keller, S. DenBaars, and U. Mishra, *Appl. Phys. Lett.* **80**, 439 (2002).
  - <sup>31</sup> S. Peters, T. Schmidling, T. Trepk, U. Pohl, J. T. Zettler, and W. Richter, *J. Appl. Phys.* **88**, 4085 (2000).
  - <sup>32</sup> R. Balmer, C. Pickering, A. Mkier, J. Birbeck, M. Saker, and T. Martin, *J. Cryst. Growth* **230**, 361 (2001).
  - <sup>33</sup> A. Bonanni, K. Schmidegg, D. Stifter, and H. Sitter, *J. Cryst. Growth* **275**, e1763 (2005).
  - <sup>34</sup> C. Simbrunner, K. Schmidegg, A. Bonanni, A. Kharchenko, J. Bethke, J. Weitok, K. Lischka, and H. Sitter, *phys. stat. sol. (a)* **203**, 1704 (2006).
  - <sup>35</sup> C. Simbrunner, K. Schmidegg, A. Bonanni, A. Kharchenko, J. Bethke, J. Weitok, K. Lischka, and H. Sitter, *J. Cryst. Growth* (in print).
  - <sup>36</sup> C. Simbrunner, A. Navarro-Quezada, K. Schmidegg, A. Bonanni, A. Kharchenko, J. Bethke, K. Lischka, and H. Sitter, *J. Cryst. Growth* (in print).
  - <sup>37</sup> A. Bonanni, K. Schmidegg, A. Montaigne-Ramil, H. Sitter, D. Stifter, and K. Hingerl, *J. Vac. Sci. Technol. B* **21**, 1825 (2003).
  - <sup>38</sup> M. Lampalzer, K. Volz, W. Treutmann, S. Nau, T. Torunski, K. Megges, J. Lorberth, and W. Stolz, *J. Cryst. Growth* **248**, 474 (2003).
  - <sup>39</sup> K. Sato, H. Katayama-Yoshida, and P. Dederichs, *Jpn. J. Appl. Phys.* **44**, L948 (2006).
  - <sup>40</sup> M. Jamet, A. Barski, T. Devillers, V. Poydenot, R. Dujardin, P. Bayle-Guillemaud, J. Rothmann, E. Bellet-Amalric, A. Marty, J. Cibert, et al., *Nat. Mat.* **5**, 653 (2006).
  - <sup>41</sup> B. Eck, R. Dronskowski, M. Takahashi, and S. Kikkawa, *J. Mater. Chem.* **9**, 1527 (1999).
  - <sup>42</sup> J. Gallego, D. Boerma, R. Miranda, and F. Yndurain, *Phys. Rev. Lett.* **95**, 136102 (2005).
  - <sup>43</sup> N. Gajbhiye, R. Panda, R. Ningthoujam, and S. Bhattacharyya, *phys. stat. sol. (c)* **1**, 3252 (2004).
  - <sup>44</sup> J. Gallego, S. Y. Grachev, D. M. Borsa, D. O. Boerma, D. Eciija, and R. Miranda, *Phys. Rev. B* **70**, 115417 (2004).
  - <sup>45</sup> D. Keavney, D.F.Storm, J. W. Freeland, I. L. Grigorov, and J. C. Walker, *Phys. Rev. Lett.* **74**, 4531 (1995).
  - <sup>46</sup> D. Jiang and E. A. Carter, *Phys. Rev. B* **70**, 064102 (2004).
  - <sup>47</sup> Z.-P. Shi, J. F. Cooke, Z. Zhang, and B. M. Klein, *Phys. Rev. B* **54**, 3030 (1996).
  - <sup>48</sup> D. Rechanbach and H. Jacobs, *J. Alloys Compd.* **235**, 15 (1996).
  - <sup>49</sup> Z. Bougrioua, M. Azize, A. Jamenez, A. Braña, P. Lorenzini, B. Beaumont, E. Muñoz, and P. Gibart, *phys. stat. sol. (c)* **2**, 2424 (2005).
  - <sup>50</sup> S. Heikman, S. Keller, S.P.DenBaars, and U. Mishra, *Appl. Phys. Lett.* **81**, 439 (2002).
  - <sup>51</sup> A. Polyakov, N. Smirnov, A. Govorkov, A. Shlensky, K. McGuire, E. Harley, L. McNeil, R. Khanna, S. Pearton, and J. Zavada, *phys. stat. sol. (c)* **7**, 2476 (2005).
  - <sup>52</sup> V. Gorodyskiy, K. Zdansky, L. Pekárek, and S. Vacková, *Semicond. Sci. Technol.* **19**, 203 (2004).
  - <sup>53</sup> M. Wegscheider (unpublished data).
  - <sup>54</sup> K. Korona, *Phys. Rev. B* **65**, 235312 (2002).
  - <sup>55</sup> A. Wysmolek, K. Korona, R. Stepniewski, J. Baranowski, J. Błoniarz, M. Potemski, R. Jones, D. Look, J. Kuhl, S. Park, et al., *Phys. Rev. B* **66**, 245317 (2002).
  - <sup>56</sup> B. Monemar, *J. Phys.: Condens. Matter* **13**, 7011 (2001).
  - <sup>57</sup> S. Bishop, in *Deep Centers in Semiconductors*, edited by S. Pantelides (Gordon and Breach, 1992), p. 667.
  - <sup>58</sup> J. Baur, K. Maier, M. Kunzer, U. Kaufmann, J. Schneider, H. Amano, I. Akasaki, T. Detchprohm, and K. Hiramatsu, *Appl. Phys. Lett.* **64**, 857 (1994).
  - <sup>59</sup> R. Heitz, A. Hoffmann, and I. Broser, *Phys. Rev. B* **45**, 8977 (1992).
  - <sup>60</sup> E. Malguth, A. Hoffmann, and X. Xu, *Phys. Rev. B* **74**, 165201 (2006).
  - <sup>61</sup> M. Kiecana, H. Przybylińska, and T. Dietl (unpublished

- data).
- <sup>62</sup> M. Venkatesan, C. B. Fitzgerald, J. G. Lunney, and J. M. D. Coey, Phys. Rev. Lett. **93**, 177206 (2004).
  - <sup>63</sup> A. Zunger, in *Solid State Physics*, edited by F. Seitz and D. Turnbull (Academic Press, New York, 1986), vol. 39, pp. 275–464.
  - <sup>64</sup> T. Dietl, Nature Mat. **5**, 673 (2006).
  - <sup>65</sup> D. W. Abraham, M. M. Frank, and S. Guha, Appl. Phys. Lett. **87**, 252502 (2005).
  - <sup>66</sup> J.-Y. Koo, J.-Y. Yi, C. Hwang, D.-H. Kim, and S. Lee, Phys. Rev. B **52**, 17269 (1995).
  - <sup>67</sup> Quantum Design, 6325 Lusk Boulevard, San Diego, CA 92121-3733, USA.
  - <sup>68</sup> One of us (MS) gratefully acknowledges the substantial contribution of dr W. Van Roy and his IMEC team in the preparation of the Si strips.
  - <sup>69</sup> The GE/IMI 7031 varnish is obtained from Cambridge Magnetic Refrigeration, Cambridge, CB5 8HR, UK. One of us (MS) is indebted to K. Edmonds for providing samples for testing.
  - <sup>70</sup> A. Zieba, Rev. Sci. Instr. **64**, 3352 (1993).
  - <sup>71</sup> P. Stamenov and J. M. D. Coey, Rev. Sci. Instr. **77**, 015106 (2006).
  - <sup>72</sup> B. H. Blott and G. J. Daniell, Meas. Sci. Technol. **4**, 462 (1993).